Research Square

Preprints are preliminary reports that have not undergone peer review.
They should not be considered conclusive, used to inform clinical practice,
or referenced by the media as validated information.

Post-Transplant Gut Dysbiosis is a Targetable Axis

Bing Ma

bma@som.umaryland.edu

University of Maryland, Baltimore

Allison Kensiski
University of Maryland, Baltimore

Long Wu
University of Maryland, Baltimore

Samuel Gavzy
University of Maryland, Baltimore

Tianshu Zhang
University of Maryland, Baltimore

Issac Chaudry
University of Maryland, Baltimore

Michael France
University of Maryland, Baltimore

Hnin Wai Lwin
University of Maryland, Baltimore

Marina WillsonShirkey
University of Maryland, Baltimore

Brendan Lohmar
University of Maryland, Baltimore

Wenji Piao
University of Maryland, Baltimore

Valeria Mas
University of Maryland, Baltimore

Jonathan Bromberg
University of Maryland, Baltimore

Research Article

Keywords: Gut microbiome, gut-heart axis, immunomodulation, Immunosuppression-associated dysbiosis, Cardiac transplantation, Lymph node stromal remodeling

Posted Date: November 5th, 2026

DOI: https://doi.org/10.21203/rs.3.rs-11272317/v1

License: This work is licensed under a Creative Commons Attribution 4.0 International License.
Read Full License

Additional Declarations: No competing interests reported.

Post-Transplant Gut Dysbiosis is a Targetable Axis

Bing Ma[1,2]*, Allison Kensiski[3,4], Long Wu[3,4], Samuel Gavzy[3,4], Tianshu Zhang[3], Issac Chaudry[1, 5], Michael France[1,2], Hnin Wai Lwin[1], Marina WillsonShirkey[3,4], Brendan Lohmar[3,4], Wenji Piao[4], Valeria Mas[3,4], Jonathan Bromberg[2,3,4]*

[1]Center for Advanced Microbiome Research and Innovation, Institute of Genome Sciences, University of Maryland School of Medicine, Baltimore, MD 21201, United States; [2]Department of Microbiology and Immunology, University of Maryland School of Medicine, Baltimore, MD 21201, United States; [3]Department of Surgery, University of Maryland Medical Center, Baltimore, MD 21201, United States; [4]Center for Vascular and Inflammatory Diseases, University of Maryland School of Medicine, Baltimore, Maryland, Maryland, 21201, United States; [5]Department of Biochemistry and Molecular Biology University of Maryland School of Medicine, Baltimore, Maryland, Maryland, 21201, United States

* Corresponding authors

Bing Ma: bma@som.umaryland.edu

Jonathan S. Bromberg: JBromberg@som.umaryland.edu

Key words: Gut microbiome, gut-heart axis, immunomodulation, Immunosuppression-associated dysbiosis, Cardiac transplantation, Lymph node stromal remodeling

ABSTRACT

Long-term graft attrition remains a critical challenge despite maintenance immunosuppression, which perturbs intestinal immune homeostasis and microbial communities, which may contribute to vascular inflammation and chronic graft injury. We previously identified *Muribaculaceae* expansion as a shared feature of long-term exposure to multiple distinct immunosuppressant classes in the murine gut microbiome. In this study, using a fully MHC-mismatched mouse heart transplant model under chronic tacrolimus treatment, we tested whether oral administration of the protolerogenic *Bifidobacterium pseudolongum subsp. globosum* (*Bifido*) or pro-inflammatory *Desulfovibrio desulfuricans* (*Desulfo*) could redirect this dysbiotic state and affect graft fate. Longitudinal metagenomic and metabolomic profiling showed an ordered tacrolimus-associated microbial succession that culminated in sustained *Muribaculaceae* enrichment with coordinated luminal and circulating metabolic remodeling. *Bifido*, but not *Desulfo*, redirected the community trajectory by reducing *Muribaculaceae* enrichment, increasing selected fermentative commensals, and establishing metabolites linked to epithelial and immune regulation, including kynurenic acid and N-acetylspermine. Spatial transcriptomics showed that *Bifido* partially attenuated early tacrolimus-induced colonic metabolic, stress, and epithelial-remodeling programs while later selectively reprogramming ileal antimicrobial defense, crypt-proximal metabolic adaptation, and mucosal humoral immunity. These changes were accompanied by minimal graft vasculitis and fibrosis, increased Foxp3^{+} regulatory T-cell localization in mesenteric and peripheral lymph nodes (LNs), and partial preservation of tolerogenic stromal laminin α4:α5 organization. In contrast, *Desulfo*-treated mice

retained *Muribaculaceae* enrichment and developed progressive vascular injury. In an exploratory human-to-mouse fecal microbiota transfer (FMT) experiment, chronic allograft vasculopathy (CAV)-associated donor stool promoted expansion of endogenous murine *Muribaculaceae* and a distinct microbial functional state, together with increased graft fibrosis, T cell infiltration, LNs remodeling, and vasculitis. Whereas non-CAV donor stool favored *Bifido* enrichment and was associated with lessened graft pathology. Together, these findings provide proof of principle that the immunosuppressant-perturbed gut ecosystem is a targetable axis, supporting novel adjunct therapies that complement immunosuppression and mitigate chronic graft injury.

Introduction

Heart transplantation has achieved excellent short-term survival with modern immunosuppressive regimens, yet long-term graft attrition remains a critical challenge. A principal cause of late graft failure is chronic rejection manifested as chronic allograft vasculopathy (CAV), a diffuse, concentric, immune-mediated obliterative arteriosclerosis that affects both epicardial and intramyocardial vessels[1, 2]. CAV develops in approximately 30% of recipients within 5 years and approaches 50% by 10 years after transplantation[3, 4]. Intravascular ultrasound studies reveal subclinical intimal thickening in most grafts by the end of the first year, indicating that vasculopathy begins earlier than other clinical indicators[5]. Current immunosuppressive regimens incompletely prevent chronic vascular injury, inflammation, fibrosis, and metabolic dysregulation while contributing to infection, malignancy, or drug-associated end-organ toxicity[6, 7].

Tacrolimus (FK506) is the cornerstone of maintenance immunosuppression after heart transplantation[8, 9]. However, tacrolimus, like other immunosuppressants, is not antigen-specific and acts broadly across immune and non-immune compartments with potential effects on intestinal immune homeostasis, epithelial function, microbial ecology, and host-microbial metabolism[10-12]. We previously found that tacrolimus, along with four other classes of immunosuppressants (cyclosporine, sirolimus, mycophenolate mofetil, and corticosteroids), induces gut dysbiosis in naïve mice and drives a convergent expansion of *Muribaculaceae*[13, 14]. Species in *Muribaculaceae* (or S24-7) are dominant members of the murine gut microbiota with broad saccharolytic and mucus-associated carbohydrate-utilization capacity[15-17]. Their metabolic versatility may confer a competitive advantage in disrupted gut environments, and enrichment of

specific *Muribaculaceae* taxa has been causally linked to insulin-dependent diabetes and impaired glucose metabolism in mice[18, 19]. The consistent enrichment of *Muribaculaceae* after treatment with different immunosuppressant classes suggests that chronic immune suppression may impose a general shared ecological selection pressure on the intestinal ecosystem. It is not known if counteracting immunosuppression induced gut dysbiosis can mitigate subsequent graft injury.

Microbial metabolism provides a plausible mechanism by which an immunosuppressant-conditioned intestinal ecosystem could influence distant vascular and immune phenotypes. Gut microbial activity contributes to circulating metabolites that affect endothelial activation, platelet function, inflammation, and renal-metabolic stress. For example, trimethylamine N-oxide (TMAO), originating from the hepatic oxidation of gut microbial produced trimethylamine (TMA), has been linked to atherosclerosis, platelet hyperreactivity, thrombosis, and adverse cardiovascular outcomes[20, 21]. Phenylacetylglutamine (PAGln), a host-conjugated product of microbial phenylalanine metabolism, augments platelet responsiveness through adrenergic receptor signaling[22]. Conversely, microbial polyamine and tryptophan metabolites can shape epithelial and antigen-presenting cell function and the balance between tolerogenic and effector immune programs[23, 24]. Defining how chronic immunosuppression reshapes this local-to-systemic metabolic interface may reveal mechanisms linking intestinal dysbiosis to chronic allograft injury.

The intestinal epithelium is a spatially structured environment that acts as a central interface through which the luminal microbiota can influence mucosal and systemic immunity. Microbial activities may also influence LN stromal organization and

leukocyte positioning, thereby shaping the regulatory and effector niches in which alloimmune responses are organized[13, 14]. Spatial transcriptomics therefore offers a means to identify the intestinal niches in which microbial activity reshapes epithelial and mucosal immune programs.

Here, we used a fully allogeneic murine heart transplant model maintained on daily tacrolimus [25, 26] to test whether oral administration of a protolerogenic *Bifidobacterium (Bifido)* could redirect post-transplant dysbiosis and attenuate chronic graft injury relative to pro-inflammatory *Desulfovibrio* (*Desulfo)* or vehicle control (no bacteria). We integrated longitudinal metagenomic and metabolomic profiling with spatial transcriptomics of the intestine, immune and stromal analyses of LNs, and graft histopathology. To explore translational relevance, we performed human-to-mouse fecal microbiota transplant (FMT) using stool from cardiac-transplant recipients with or without CAV, and healthy donors. This design tested whether a tacrolimus-conditioned gut ecosystem constituted a modifiable axis linking microbial communities, epithelial adaptation, metabolic remodeling, immune organization, and chronic allograft injury. This proof-of-principle study evaluated the gut ecosystem as a modifiable adjunctive target to complement immunosuppression and limit chronic graft injury.

Results

Tacrolimus-associated microbiome succession after cardiac transplantation

We previously showed that prolonged exposure to five mechanistically distinct immunosuppressant classes each induced a conserved dysbiotic state marked by reduced diversity and *Muribaculaceae* expansion in naïve mice[13]. Here, we examined whether this signature occurs in a fully MHC-mismatched cardiac-transplant model maintained on daily low-dose tacrolimus[25, 26]. Longitudinal fecal microbiome profiling from day 0 to day 40 revealed a time-structured succession of the post-transplant gut microbiome (**Figure 1A, Supplemental Table 1**). Changes in microbial family-level composition showed three broad temporal patterns: (i) early depletion, (ii) transient early expansion, and (iii) late or sustained enrichment. *Akkermansiaceae* (e.g. *Akkermansia muciniphila*) was nearly absent on day 0, peaked on day 7 and declined rapidly, becoming nearly undetectable by day 14 (**Figure 1B**). *Bacteroidaceae* (e.g. *Bacteroides thetaiotaomicron*) similarly dropped by day 7 and remained low thereafter. *Enterobacteriaceae* decreased to near-zero by day 7, and *Lactobacillaceae* declined sharply by day 3. In contrast, several *Lachnospiraceae* (e.g.14-2, *Acetatifactor*, 1XD42-69, 1XD8-76) increased rapidly and peaked at day 7, indicating a transient fermentative response following loss of primary mucin- and polysaccharide-utilizing taxa. *Acutalibacteraceae* also showed modest early increases by day 7 but did not persist.

Muribaculaceae showed the most prominent expansion, peaking near day 14 and remaining dominant through day 40 with only a modest decline after day 28 (**Supplemental Figure 1**). This pattern was driven primarily by *Duncaniella*, *CAG-873*, and *Paramuribaculum*, the same *Muribaculaceae*-associated genera identified in

chronically immunosuppressed naïve mice[13]. *Bifidobacteriaceae* (*Bifidobacterium pseudolongum*) became detected by day 21 and persisted in low relative abundance through day 40. Together, these findings demonstrated an ordered post-transplant microbial succession under chronic tacrolimus, characterized by early loss of multiple commensals, transient enrichment of selected Lachnospiraceae, and sustained *Muribaculaceae* dominance. They extend the previously observed immunosuppression-associated dysbiotic signature to a chronic cardiac allograft setting.

Longitudinal fecal metagenomes were also analyzed using HUMAnN4 to relate functional profiles to taxonomic succession. Tacrolimus-associated dysbiosis was accompanied by a structured transition in microbial metabolic potential. The early loss of *Lactobacillaceae* and other commensals coincided with the progressive depletion of hexitol fermentation to lactate, formate, ethanol, and acetate; NAD salvage to nicotinamide riboside; and polyamine biosynthesis pathways (**Figure 1C**). Reaction-level profiles similarly showed reduced D-lactate dehydrogenase, tryptophan synthase, and kynurenine 3-monooxygenase signals after the early time points. In contrast, expansion of *Muribaculaceae* coincided with retention or enrichment of carbohydrate-processing functions during the later dysbiotic phase (**Figure 1D**). Glycolysis III from glucose increased when *Muribaculaceae* became dominant, whereas lactate fermentation to propanoate and acetate remained detectable across the time course (**Figure 1E**). The moderate late increase in *Bifido* abundance was accompanied by recovery of the *Bifido* shunt, consistent with partial restoration of bifidobacterial carbohydrate-fermentation potential late in the time course. Several functions related to phosphatidylcholine turnover and choline release or utilization, including

phosphatidylcholine acyl editing, choline sulfatase, choline kinase, and acetylcholinesterase, also varied longitudinally. Taxonomic stratification indicated that reduced choline sulfatase abundance was driven by depletion of *Bacteroides thetaiotaomicron* (**Supplemental Figure 2**). In contrast, most of the acetylcholinesterase abundance could not be attributed to contributed a particular taxa unclassified taxa, with minor contributions from *Lachnospiraceae*. Whereas phosphatidylcholine acyl editing involved unclassified taxa and *Enterobacter hormaechei*. Chronic tacrolimus exposure was associated with convergence of fecal metagenomic functional profiles, reflected by reduced within-day Bray-Curtis separation and lower distance to day-specific centroids at later time points (**Supplemental Figure 3**). Taxonomic profiles showed a similar pattern, indicating that functional convergence accompanies taxonomic succession. Together, these data showed that a tacrolimus-associated microbiome is characterized by selective remodeling of the functional capacity. Chronic tacrolimus treatment resulted in the early depletion of commensal-associated lactate, NAD, polyamine, and tryptophan-related functions with a subsequent transition to a *Muribaculaceae*-dominant state that was enriched for carbohydrate-utilization potential.

Chronic tacrolimus drives staged gut-systemic metabolic remodeling and late host-microbial co-metabolism

We longitudinally profiled the ileal intraluminal and serum metabolomes in cardiac allograft recipient mice at day 0, after antibiotic conditioning but before transplantation and tacrolimus treatment, and at days 3 and 40 after transplantation under daily tacrolimus treatment (**Figure 2A, 2B, Supplemental Table 2A, 2B**). For

each metabolite, group differences were tested by one-way ANOVA with Tukey's honestly significant difference (HSD) post hoc pairwise comparisons and Benjamini-Hochberg FDR correction (**Supplemental Table 2C-E**). Hierarchical clustering revealed distinct metabolic states at baseline, day 3, and day 40 in both the intestinal lumen and circulation, indicating progressive temporal remodeling during the post-transplant period (**Supplemental Figure 4A, 4B**). In the intestinal lumen, this remodeling was characterized by rapid and sustained changes in selected microbial and host-microbial metabolites (**Figure 2C**; **Supplemental Figure 5A**). Kynurenic acid (KYNA) was abundant at baseline but declined sharply by day 3 and remained depleted through day 40; N-methyltyramine followed a similar trajectory. In contrast, diaminopimelic acid (DAP) increased rapidly and remained elevated, consistent with sustained bacterial cell-wall turnover during microbial community restructuring. Serum metabolites followed a parallel but distinct temporal trajectory (**Figure 2D**, **Supplemental Figure 5B**). At baseline, serum was enriched for medium- and long-chain fatty acids, including α-linolenic acid, stearidonic acid, oleic acid, myristoleic acid, palmitoleic acid, docosahexaenoic acid, and docosapentaenoic acid, together with thiol- and redox-associated metabolites. By day 3, these lipid and antioxidant pools were broadly depleted, whereas metabolites associated with tissue remodeling, amino acid turnover, nitrogen metabolism, and oxidative stress increased, including allysine, 4-hydroxyproline, lysine, aminoadipic acid, ornithine, α-aminobutyric acid, L-cystine, homoarginine, imidazolepropionic acid, and 1-methyl-4-imidazoleacetic acid. By day 40, the serum metabolome had transitioned to a chronic state marked by the accumulation of microbial and host–microbiome co-metabolic products, including trimethylamine N-

oxide (TMAO), phenylacetic acid (PAA), phenyllactic acid (PLA), and phenylacetylglutamine (PAGln). Together, these findings showed that the post-transplant period under chronic tacrolimus was accompanied by a staged metabolic trajectory, with early luminal depletion of selected microbial metabolites and systemic lipid-redox disruption followed by late accumulation of host-microbiome co-metabolites linked to vascular and inflammatory pathways.

We next focused on metabolites that changed across both the intestinal lumen and circulation to identify coordinated gut-systemic metabolic responses. One of the most prominent was TMAO, which accumulated at day 40 in both compartments (**Figure 2E**). In the gut lumen, late increases in phosphocholine and glycerophosphocholine were accompanied by increased trimethylamine (TMA) and TMAO, while serum TMAO increased in parallel. This coordinated pattern was consistent with enhanced engagement of the choline-TMA-TMAO host–microbial co-metabolic axis during chronic tacrolimus exposure. A second cross-compartment signature involved phenylalanine- and tyrosine-derived metabolites (**Figure 2F**). In the gut lumen, PLA, 3-(4-hydroxyphenyl)lactate, and tyramine increased by day 40, together with a late increase in PAGln. In serum, PAA and the related aromatic acids 2-hydroxyphenylacetic acid and 4-hydroxyphenylacetic acid increased markedly, accompanied by increased glutamine and PAGln. The accumulation of aromatic lactates in the lumen was consistent with increased representation of reductive aromatic amino acid metabolism, whereas the concurrent systemic enrichment of PAA-, hydroxyphenylacetate-, and PAGln-related metabolites indicated broader remodeling of phenylalanine and tyrosine co-metabolism. Together, these coordinated luminal and

circulating signatures showed that tacrolimus-associated microbial succession was accompanied by late remodeling of choline and aromatic amino acid metabolism, linking intestinal ecological change to systemic metabolic pathways with potential relevance to vascular and inflammatory injury.

Pro-tolerogenic *Bifido* reshapes the tacrolimus-conditioned gut microbiome and limits *Muribaculaceae* dominated dysbiosis

To determine if intervening with oral bacterial gavage could reshape the post-transplant gut ecosystem under chronic tacrolimus treatment, mice were orally gavaged with *Bifido*, *Desulfo*, or PBS control (tacrolimus-only, TAC) on day 0 followed by cardiac allograft transplantation and daily tacrolimus treatment starting on day 0. (experimental design in **Figure 3A**). This experiment was designed to test whether targeted bacterial supplementation could reshape the tacrolimus-conditioned gut ecosystem. We hypothesized inoculation with protolerogenic bacteria would counteract immunosuppressant-associated dysbiosis while inoculation with proinflammatory bacteria would exacerbate dysbiosis. We performed trajectory analysis using PCoA connected by temporal vectors, which revealed that the *Bifido* and *Desulfo* groups followed distinct trajectories, with the TAC and *Desulfo* groups exhibiting similar trajectories. (**Figure 3B**). PCA further supported this observation and showed that by day 40 the *Bifido* group diverged from the *Desulfo* and control groups, with separation becoming more pronounced over time (**Figure 3C**). Time-resolved ordination further showed that *Bifido*-treated mice formed a distinct community by day 7 and remained separated from tacrolimus-only and *Desulfo*-treated mice throughout the study period (**Supplemental Figure 6**).

We visualized changes in microbial community composition in response to bacterial gavage with a species-level heatmap ordered by time and group (**Supplemental Figure 7**). *Bacteroides thetaiotaomicron* remained one of the most abundant taxa through day 28 in mice gavaged with *Bifido*. The *Bifidobacterium* itself peaked immediately post-gavage, then declined to a low but persistent level, suggesting that repeated administration may be needed to sustain high-level colonization. As *Bifido* relative abundance waned, several *Muribaculaceae* lineages, which were enriched in the TAC and *Desulfo* groups, expanded in a reciprocal manner. Early after gavage, *Bifido* relative abundance was highest while lineages in Muribaculaceae (*Duncaniella*, *Paramuribaculum*, and CAG-873) remained low. As *Bifido* relative abundance declined between days 7 and 14, these *Muribaculaceae* lineages increased (**Figure 3D**). We next used longitudinal mixed-effects models incorporating treatment group and sampling time as fixed effects and mouse as a subject-level effect, to identify taxa that consistently differed between treatment groups. Relative to tacrolimus-only controls, *Bifido* treatment was associated with lower relative abundance of multiple *Muribaculaceae* lineages, including *Duncaniella, CAG-485, UBA7173,* and *CAG-873*, while favoring taxa from *Bacteroidaceae, Lachnospiraceae,* and *Ruminococcaceae* (**Supplemental Figure 8A**). Similarly, compared to the *Desulfo* group, *Bifido* gavage enriched not only for *Bifido* itself, but also for *CAG-180, UBA2882, Bacteroides, Prevotella, Ruminiclostridium, COE1,* and *1XD8-76*. Conversely, *Desulfo*-gavaged mice were enriched for several Muribaculaceae lineages, including *Duncaniella, CAG-485, UBA7173, Paramuribaculum, Muribaculum,* and *CAG-873*, together with *Emergencia, MGG50002,* and *UBA7001* (**Supplemental Figure 8B**). *Desulfo* and control groups

exhibited only modest between group differences. Together, these results showed that *Bifido* redirected the tacrolimus-conditioned community away from a *Muribaculaceae*-enriched state.

To assess the reproducibility of microbiome remodeling after bacterial supplementation, we repeated the experiment in an independent mouse cohort under identical transplantation, antibiotic-conditioning, and chronic tacrolimus conditions. Although the magnitude and temporal pattern of *Bacteroides thetaiotaomicron* differed between experiments, the principal response was reproducible (**Supplemental Figure 9A, 9B**). In both cohorts, the gavaged *Bifidobacterium* expanded transiently after gavage, *Firmicutes*, particularly *Clostridales*, progressively increased, and *Muribaculaceae* enrichment was suppressed relative to tacrolimus-only controls. This pattern was also consistent with our prior transplant study, in which early *Bifido* administration transiently reduced *Muribaculaceae* abundance before re-expansion at later time points ([25]and adapted in **Supplemental Figure 9C**). Adjusted association modeling of the combined replicate datasets identified taxonomic groups associated with *Bifido* relative abundance (**Figure 3E**). *Clostridiaceae* and *Peptostreptococcaceae* showed the strongest positive associations with *Bifido*, whereas *Duncaniella* and *Muribaculum* showed inverse associations. Together, these data demonstrated that *Bifido* reproducibly redirected the tacrolimus-conditioned endogenous microbiome beyond transient addition of itself. The later rebound of *Muribaculaceae* after *Bifido* decline indicated that this compositional redirection was not fully durable after a single administration, so that repeated administration may be needed.

Bifido redirects the functional and metabolic state of the tacrolimus-conditioned gut ecosystem

We next asked whether the taxonomic remodeling induced by *Bifido* was accompanied by a coordinated shift in microbial functional potentials. Metagenomic pathway profiles from two independent cohorts showed that *Bifido* gavage shifted the tacrolimus-conditioned microbiome into a distinct functional state. Shared pathways, defined by a pooled FDR < 0.10 and concordant *Bifido* versus control effect direction in both cohorts, were visualized in a row-scaled heatmap (**Figure 4A**). Across both experiments, the largest functional transition occurred between the pre-gavage baseline and the post-transplant period. Most pathways were low at day 0 and increased after transplantation and *Bifido* exposure, with broadly similar directionality across cohorts. The magnitude of change differed between experiments, consistent with the baseline community differences observed in the taxonomic analyses. The adjusted mixed-effects model identified a set of *Bifido*-associated functional pathways that consistently distinguished *Bifido*-treated mice from PBS/tacrolimus controls across both experiments (**Figure 4B**). Pathways increased in *Bifido*-treated mice were dominated by bacterial biosynthetic functions, with the largest effects observed for dTDP-N-acetylviosamine biosynthesis and bacterial phospholipid biosynthesis, followed by L-isoleucine biosynthesis II, glycogen biosynthesis from ADP-D-glucose, and L-valine biosynthesis. These changes indicated enrichment of selected cell-envelope, membrane, carbohydrate-storage, and branched-chain amino-acid biosynthetic functions. In contrast, pathways reduced in *Bifido*-treated mice were broader and included UDP-N-acetyl-D-galactosamine biosynthesis II, norspermidine biosynthesis, L-tyrosine

degradation I, terminal O-glycan residue modification, aerobic respiration I, Entner-Doudoroff carbohydrate metabolism, assimilatory sulfate reduction, sulfate assimilation and cysteine biosynthesis, unsaturated fatty-acid biosynthesis, and queuosine biosynthesis. These decreases were functionally distinct from the pathways enriched after *Bifido*, arguing against a nonspecific suppression of microbial metabolic potential. Instead, *Bifido* selectively reduced functions associated with sulfur assimilation, aerobic respiratory capacity, nucleotide/tRNA modification, and selected glycan and lipid pathways.

Taxonomic attribution of stratified pathways showed that these functional shifts were distributed across the endogenous community rather than dominated by the gavaged *Bifido* strain (**Figure 4C**). *Bifido* contributed to selected amino-acid biosynthetic pathways but accounted for only a subset of the overall functional shift. Contributions to *Bifido*-enriched pathways were otherwise distributed among Bacteroides, including *B. thetaiotaomicron*, and multiple unclassified taxa. Conversely, pathways reduced in *Bifido*-treated mice were attributed broadly to *Akkermansia*, *Enterobacteriaceae*, Muribaculaceae, *Akkermansia*, and *Clostridia*, and a considerable portion of unclassified taxa. Many *Muribaculaceae* and *Clostridial* contributors remain unresolved at the species level. Together, these data showed that *Bifido* reorganized community functional potential away from sulfur-assimilation and aerobic-respiratory programs and toward selected carbohydrate-storage, branched-chain amino-acid, membrane, and cell-envelope biosynthetic functions. Thus, transient *Bifido* exposure acted as an ecological perturbation that redirected the endogenous tacrolimus-

conditioned microbiome, propagating functional changes through the remodeled community rather than through the administered strain alone.

We next determined whether this community-level functional redirection was reflected in measurable metabolic output. Intraluminal stool and serum metabolomes were profiled at days 3 and 40 after *Bifido*, *Desulfo*, or PBS (tacrolimus-only, TAC) gavage under chronic tacrolimus treatment (**Supplemental Table 3A, 3B**). Consistent with the metagenomic evidence of functional remodeling, *Bifido* produced a distinct luminal metabolomic profile at both day 3 and day 40, distinct from TAC controls and *Desulfo*-treated mice (**Figure 5A, B**). This separation was most evident in stool, and no FDR-significant metabolites were detected in paired serum, indicating that the dominant metabolic consequence of *Bifido* gavage was localized to the gut lumen within the sampling window and gavage schedule. At day 3, four metabolites were specifically elevated in *Bifido*-treated mice relative to both TAC controls and *Desulfo*-treated mice, including kynurenic acid, N-acetylspermine, orotic acid, and N6,N6-dimethyladenosine (**Figure 5C**). These early changes suggested rapid engagement of tryptophan metabolism, acetylated polyamine metabolism, and nucleotide-related pathways. By day 40, N-acetylspermine remained specifically elevated in *Bifido*-treated mice, while tryptamine increased and 3-(3-hydroxyphenyl)propanoic acid decreased (**Figure 5D**). To distinguish transient from durable *Bifido*-associated metabolites, we fit longitudinal models across the shared day 0 baseline and both post-gavage timepoints. Fourteen metabolites showed significant group-by-day effects, with N-acetylspermine representing the most consistent *Bifido*-associated metabolite across timepoints, whereas kynurenic acid was primarily an early day 3 feature (**Figure 5E, Supplemental**

Table 4C). Together, the metagenomic and metabolomic analyses support a coherent model in which *Bifido* gavage did not simply engraft as a dominant functional strain. Instead, transient *Bifido* exposure reorganized the tacrolimus-conditioned microbial community, producing a local metabolic program predominantly within gut lumen.

Bifido attenuates early tacrolimus-associated colonic stress-metabolic programs and reprograms late ileal epithelial, metabolic, and humoral responses

To determine whether *Bifido* modifies host intestinal responses in parallel with microbiome changes, we performed 10x Visium spatial transcriptomics on ileum and colon from PBS tacrolimus-control (TAC) and *Bifido*-treated mice (**Supplemental Table 4A**). Visium spots were annotated as apical or basal epithelial regions based on spatial localization and transcriptomic clustering, and these annotations were projected onto the tissue sections. Across all 9,912 well-expressed genes, apical and basal epithelial compartments explained 29.9% of variance, ileum or colon tissue type 19.9%, and treatment group 4.8%, and the remaining were residual or unexplained plus interaction effects and genes specific to individual mice. PCA of the resulting compartment-level expression profiles showed that the epithelial compartment was the dominant source of transcriptional variation, separating apical from basal regions across treatment groups, with additional separation by tissue type (**Figure 6A, 7B**). We focused on epithelial-associated regions and annotated apical and basal epithelial compartments to assess whether transcriptional responses were spatially organized along the intestinal epithelial layers (**Figure 6C, Supplemental Figure 10**). Using the variance decomposition of the Hallmark module scores, most modules were compartment and/or tissue-dominated (**Supplemental Table 4B**). For example, proliferation modules were driven

overwhelmingly by compartment, consistent with basal crypt regions being the proliferative zone and apical/villus regions being post-mitotic. We therefore focused on the 15 modules with the greatest treatment-group-associated variance relative to compartment and tissue (**Supplemental Figure 11**), together with tacrolimus-responsive intestinal genes identified in our previous transcriptomic study[13]. Differential expression analysis was then performed within each spatial compartment and time point to first define TAC-associated intestinal responses and subsequently compare *Bifido*-treated mice with TAC controls at days 3 and 40 to identify *Bifido*-associated spatial transcriptional programs.

We first examined how *Bifido* altered the dominant metabolic response in the colonic apical epithelium. At day 3, cholesterol homeostasis, peroxisome, and bile acid metabolism converged with a common TAC-high, *Bifido*-lower pattern (**Figure 6D, Supplemental Figure 12**). TAC induced a coordinated cholesterol-homeostasis transcriptional program in the colonic apical compartment at day 3, increasing all 15 module genes, 14 of which were significantly altered relative to baseline. This response included coordinated induction of *Hmgcs1*, *Mvd*, *Pmvk*, *Fdft1*, *Sqle*, *Sc5d*, and Ldlr. STRING analysis showed that the sterol-biosynthesis genes formed a connected functional network (**Supplemental Figure 13**). *Bifido* shifted 93% of these genes in the direction opposite to TAC, reducing the median residual effect to 47% of the TAC-associated change without fully restoring expression to baseline. Similarly, TAC significantly altered 19 of 27 peroxisome genes and 20 of 27 bile acid metabolism genes, and *Bifido* opposed the TAC-associated direction for 96% of genes in each module. The modules converged through shared genes including *Fabp6*, *Sult2b1*,

Nr1i2, and multiple *Pex* genes, together with sterol- and nuclear receptor-associated nodes such as *Dhcr24* and *Rxra*, supporting a coordinated sterol-bile acid-peroxisomal program regulation at the colonic apical site. *Bifido* gavage also induced a coherent oxidative-phosphorylation network relative to TAC in the colonic apical compartment at day 3. In parallel, the reactive oxygen species (ROS) module showed selective, nonuniform remodeling of antioxidant genes, including *Sod1*, *Cat*, *Gpx3*, *Prdx1*, *Prdx6*, and *Gclm*. Together, these findings showed that *Bifido* reprogrammed the early colonic apical response by partially attenuating TAC-induced sterol-bile acid-peroxisomal programs, enhancing mitochondrial respiratory gene expression and selectively remodeling antioxidant defenses.

We next examined whether *Bifido* altered TAC-associated colonic apical signaling programs related to innate sensing, cellular stress, growth regulation, and epithelial remodeling. The PI3K-AKT-mTOR, TNFα-NF-κB, and TGF-β/BMP modules showed their strongest treatment-associated signals in the colonic apical compartment at day 3, with broad TAC induction followed by partial attenuation with *Bifido* (**Figure 7A, Supplemental Figure 14A**). TAC altered 28 of 30 PI3K-AKT-mTOR module genes, which linked innate-sensing components, including *Myd88*, *Tbk1*, *Ripk1*, *Traf2*, and *Map3k7*, with PI3K-AKT-mTOR-associated growth and nutrient-regulatory genes such as *Pten*, *Tsc2*, *Rptor*, and *Pik3r3*. *Bifido* opposed the TAC-associated direction for 97% of these genes, reducing the median residual effect to 52%, consistent with attenuation of a coordinated sensing–adaptation program. In the TNFα–NF-κB module, TAC altered 64 of 65 genes, including core NF-κB components and immediate-early stress-response genes, and *Bifido* shifted 94% in the opposite direction with a median residual effect of

58%. TAC also altered all 23 TGFβ/BMP genes, including *Smad1*, *Smad3*, *Smad7*, *Bmpr2*, *Id1*, *Id2*, *Pmepa1*, and *Tjp1*, and *Bifido* opposed the TAC direction for 96%, reducing the median residual effect to 53%. A parallel protein-secretion module supported the same response. TAC altered 28 of 32 module genes, including core vesicle-trafficking machinery, and all shifted in the opposite direction after *Bifido*, with a median residual effect of 53%. STRING analysis further showed a connected SMAD-centered TGF-β/BMP network including pathway activation, differentiation, and negative-feedback regulators, suggesting that TAC broadly engaged an epithelial remodeling program and stress-adaptation program that was partially attenuated by *Bifido* (**Figure 7D**). Together, these results indicated that *Bifido* broadly dampened, but did not completely normalize, a TAC-associated colonic surface program integrating innate sensing, NF-κB/immediate-early stress responses, growth and nutrient regulation, TGF-β/BMP signaling, and secretory-trafficking remodeling.

We then assessed how *Bifido* reprogrammed spatially distinct intestinal functions beyond the early colonic apical response. At day 40, TAC suppressed most ileal apical α-defensins and *Lyz1*, and *Bifido* shifted only a subset toward pretreatment levels while leaving much of this suppression intact (**Figure 7B**). In contrast, TAC strongly induced *Reg3b* and *Reg3g*, and *Bifido* further increased both, indicating selective amplification of a distinct C-type lectin antibacterial response. Thus, *Bifido* gavage reprogrammed rather than broadly restored ileal antimicrobial defense. *Bifido* established a broad mTORC1-associated transcriptional program spanning glycolysis, serine, one-carbon and amino acid metabolism, proteasomal processing, and ER proteostasis, including *Gapdh, Eno1, Phgdh, Shmt2, Asns, Psmc6, Psmd14, Nupr1, Ddit3, Edem1,* and *Sdf2l1*

(**Figure 7C**). STRING analysis further revealed an interconnected functional network linking metabolic regulation with protein processing and ER proteostasis, supporting a coordinated cellular adaptation rather than isolated gene-level changes (**Figure 7E**). In the ileal basal/deeper-wall compartment at day 40, *Bifido* induced a broad mTORC1-associated transcriptional program relative to TAC controls. Among the 50 module genes included because they differed in at least one of the two contrasts, only two were significantly altered by TAC relative to pretreatment baseline. Thus, this pattern reflects induction of a distinct *Bifido*-associated state rather than reversal of a TAC-induced perturbation. In the same ileal basal compartment, *Bifido* also increased expression of fatty acid metabolism genes relative to TAC controls, including *Acsl5*, *Cpt2*, *Acadl*, *Eci1*, *Eci2*, *Decr1*, *Crat*, *Hsd17b4*, and *Mcee*, consistent with greater transcriptional capacity for mitochondrial fatty acid oxidation **(Supplemental Figure 14B**). *Fabp2* remained strongly suppressed, indicating that *Bifido* did not broadly restore mature absorptive-enterocyte functions but instead established a selective crypt-proximal metabolic state. In the colonic basal/deeper-wall compartment, *Bifido* more closely normalized a TAC-associated colonic basal contractile signature at day 40 **(Supplemental Figure 14C**). TAC increased smooth-muscle and myofibroblast-associated genes, including *Acta2, Tagln, Myh11, Mylk, Myl9, Tpm1, Tpm2, Actg2,* and *Ppp1r12b*, whereas *Bifido* shifted all 12 module genes opposite to the TAC direction, reducing the median residual effect to 24%. Spatial mapping localized the highest module scores to the muscularis boundary, supporting a stromal or smooth-muscle origin (**Figure 7F**). These findings showed that Bifido did not uniformly reverse TAC-associated intestinal responses.

Finally, we asked whether *Bifido* elicited a spatially localized adaptive immune response in the intestine. Canonical T cell, conventional B cell, and dendritic cell marker programs showed no consistent treatment-associated signal, whereas a targeted immunoglobulin and plasma-cell module emerged in the ileal apical compartment at day 40. Five of eight module genes were already altered by TAC relative to the day 0 baseline, including strong induction of *Cd38, Igkc, Igha, Jchain,* and *Iglc2* (**Figure 7B**). All eight genes differed between *Bifido* and TAC, with seven increasing after *Bifido*, including further induction of *Cd38, Igkc, Igha,* and *Jchain* and *Bifido*-associated increases in *Iglc1, Iglc3,* and *Ighg2b*; *Iglc2* was the only gene reduced. The coordinated increase in *Igha* and *Jchain*, together with plasma-cell-associated and immunoglobulin constant-region genes, suggested that *Bifido* may enhance local antibody-secreting-cell activity and an IgA secretory program. Spatial mapping showed higher and more broadly distributed module scores throughout the ileal apical compartment after *Bifido* treatment, indicating a widespread rather than focal humoral response (**Figure 7G**). Together, these findings identified a late, spatially widespread ileal humoral response as the predominant adaptive immune program associated with *Bifido*, suggesting selective enhancement of mucosal antibody-secreting-cell activity rather than broad intestinal lymphocyte activation.

Bifido FMT mitigates graft vasculitis and preserves regulatory lymphoid and graft stromal organization under chronic tacrolimus

We next assessed whether bacterial supplementation altered graft pathology under chronic tacrolimus treatment. Histologic scoring of graft tissue showed that TAC and *Desulfo* groups exhibited significantly increased inflammation and fibrosis by day

40, whereas *Bifido* recipients were comparatively protected (**Figure 8A**). Notably, *Desulfo* showed the highest fibrosis scores as early as day 3 on trichrome-stained cardiac allograft sections, indicating rapid pathologic acceleration. We also evaluated graft vasculature at early (day 3) and late (day 40) time points using the standard cardiac graft-rejection vascular scoring system (**Figure 8B**). *Desulfo* produced rapid and escalating vascular injury, with mild perivascular lymphocytic infiltrates at day 3 that progressed to severe vasculitis by day 40 with intravascular lymphocyte accumulation and vessel wall damage. TAC followed a similar but milder progressive pattern despite immunosuppression. In sharp contrast, *Bifido* maintained minimal vascular scores at both times. These data underscored that persistent, progressive graft vasculitis can occur post-transplant, which immunosuppressants alone cannot fully mitigate, as seen clinically; whereas a protolerogenic microbiome state induced by *Bifido* gavage preserved vascular integrity and mitigated fibrotic remodeling.

To determine whether *Bifido*-associated graft protection was accompanied by changes in lymphoid immune regulation, we quantified Foxp3$^+$ Treg localization in pLNs and mLNs, focusing on the cortical ridge (CR) and high endothelial venule (HEV) regions. *Bifido* markedly increased Treg localization in the CR and around HEVs of mLNs at day 3, and this enrichment remained evident at day 40. A similar pattern was observed in pLNs, where *Bifido* significantly increased Foxp3$^+$ Tregs in both CR and HEV regions at early and late time points (**Figure 8C**, **Supplemental Figure 15A, 15B**). These findings indicated that *Bifido* promoted sustained Treg positioning within both gut-draining and systemic lymphoid niches under chronic tacrolimus treatment. Given that HEV-associated Tregs can limit inflammatory cell entry into LNs and CR-localized

Tregs can restrain antigen-driven T-cell priming, these data suggest that *Bifido*-associated protection restored a regulatory LN microenvironment.

We further examined whether *Bifido* altered the intragraft immune and stromal environment. In cardiac allografts, the laminin α4:α5 ratio declined markedly by day 40 in TAC controls, indicating progressive loss of a regulatory stromal architecture within the graft (**Figure 8D, Supplemental Figure 15C**). *Bifido* did not significantly alter this ratio at day 3, but by day 40 it preserved a significantly higher laminin α4:α5 ratio compared with TAC controls, suggesting protection from chronic graft stromal remodeling. Consistent with this, TAC controls showed a marked accumulation of intragraft $CD4^+$ T cells by day 40, whereas *Bifido* significantly reduced $CD4^+$ T cell infiltration at this late time point. $Foxp3^+$ Tregs and $CD8^+$ T cells increased over time in both TAC and *Bifido*-treated grafts, indicating that *Bifido* did not fully prevent all cellular recruitment into the graft (**Figure 8D, Supplemental Figure 15D**). Rather, its strongest intragraft effect was preservation of laminin α4:α5 organization and selective limitation of $CD4^+$ T cell accumulation. Together with the vascular scoring and fibrosis data, these findings indicated that *Bifido* mitigated chronic graft inflammatory remodeling under tacrolimus but did not eliminate late intragraft immune cell infiltration. Overall, *Bifido* gavage mitigates chronic graft inflammatory remodeling under tacrolimus by linking reduced vascular injury and fibrosis with enhanced LN regulatory positioning and partial preservation of graft stromal architecture.

<u>CAV-associated human microbiota establish distinct post-FMT ecological trajectories</u>

To extend our murine FMT observations to a translational setting, we transferred stool from cardiac transplant patients with CAV, without CAV, or from a healthy donor

554 (CAV-FMT, n=6 recipient mice; non-CAV-FMT, n=5; healthy-control FMT, n=4; **Figure**
555 **9A**). Mice received six days of broad-spectrum antibiotic conditioning[27], followed by a
556 washout period and weekly FMT for four weeks to promote sustained human microbiota
557 engraftment. Trichrome staining of graft sections showed significantly higher cardiac-
558 allograft fibrosis scores in CAV-FMT recipients compared to non-CAV (**Figure 9B, 9D**).
559 Immunohistochemistry further demonstrated increased $CD4^+$ and $CD8^+$ T-cell infiltration
560 in cardiac allografts (**Figure 9B, Supplemental Figure 16A**) and a reduced laminin
561 α4:α5 ratio in draining LNs in CAV FMT recipients (**Figure 9B**), consistent with LN
562 remodeling toward a pro-inflmmatory state. pLN similarly showed reduced laminin α4:α5
563 ratios (**Fig. 9C, Supplemental Figure 16B**), indicating more widespread lymphoid
564 stromal remodeling. Together, these findings showed that microbiota derived from CAV
565 and non-CAV recipients were associated with divergent lymphoid and graft phenotypes.
566 Whole-community longitudinal analysis showed that the most dominant
567 microbiome signal was a pronounced, concordant displacement from day 0 to day 7
568 across all three donor groups (**Figure 9E**), consistent with major early post-conditioning
569 and FMT-associated community restructuring. The microbiota subsequently continued
570 along distinct post-FMT trajectories, with day 28 and day 60 samples showing similar
571 overall community, suggesting establishment of relatively stable late community states.
572 Within these shared temporal dynamics, CAV-, non-CAV-, and healthy-control FMT
573 recipients followed distinguishable trajectories, indicating that donor-associated
574 microbiota further shaped the community state established at each post-FMT time point.
575 To identify the taxa underlying these donor-group-specific trajectories, we next
576 performed time-resolved pairwise comparisons of CAV-FMT with non-CAV-FMT and

healthy-control FMT recipients (**Supplemental Figure 17A**). Taxa differing at one or more post-FMT time points were identified, and their longitudinal trajectories were examined to determine whether these differences were transient or maintained over time. By day 7, CAV-FMT recipients already showed substantial taxonomic divergence, involving *Ruminococcus* B, *Parasutterella*, *UBA11940*, *CAG-267*, *Longibaculum*, *Duncaniella*, *Duodenibacillus*, and *Flavonifractor*, among others. These taxa remained directionally enriched in CAV recipients through day 60, although persistence and statistical significance varied. We therefore applied a group-by-time mixed model to identify genera consistently enriched in CAV across the post-FMT period relative to the combined non-CAV and healthy-control groups, with Benjamini-Hochberg correction for multiple testing. Sixteen CAV-enriched genera met prespecified criteria of FDR <0.05, >1.5-fold enrichment, and mean CAV abundance ≥0.1% (**Supplemental Figure 17B**), including *Ruminococcus* B, *Parasutterella*, *CAG-267*, *CAG-873*, *UMGS1872*, *Flavonifractor*, *Clostridium*, *Longibaculum*, and *Duncaniella*. Muribaculaceae expanded from 0.58% at baseline to 10.18%, 19.73%, and 18.86% at days 7, 28, and 60 in CAV-FMT recipients, whereas expansion was delayed in healthy-control recipients and remained lower in non-CAV recipients (**Figure 9G**). Note that *Duncaniella* and *CAG-873* were both previously identified as immunogenic taxa enriched in tacrolimus-only conditions and reduced under *Bifido* gavage. Because these murine family Muribaculaceae were in very low abundance before FMT and were not expected to derive directly from human donor stool, their expansion was most consistent with outgrowth from an endogenous murine reservoir under a permissive post-FMT ecological state. Thus, the donor-associated microbiota influenced not only which

transferred taxa persisted, but also which endogenous recipient lineages subsequently expanded. An opposing ecological pattern was observed for taxa within *Lachnospiraceae*, *Bifidobacteriaceae*, and *Ruminococcaceae*, several of which remained depleted in CAV-FMT recipients over time (**Supplemental Figure 17A**). Species-level assignments included *B. longum*, *B. pseudolongum subsp. globosum* (*Bifido*), *B. animalis*, and *B. bifidum*. *B. longum*, a human-associated species, was consistently more abundant in non-CAV recipients (**Supplemental Figure 17C**). *B. animalis* and *B. bifidum* were also detected but cannot be assigned as human- or murine-derived from species-level classification alone. Notably, *B. pseudolongum*, *Bifido* itself appeared in non-CAV FMT mice by day 28 and was maintained through day 60, suggesting acquisition from the murine endogenous reservoir once permissive conditions induced by FMT were created. Together, these findings indicated that post-FMT colonization was governed by ecological selection rather than donor detection alone.

CAV-associated microbiota establish distinct functional states after human FMT

We next asked whether the divergent taxonomic trajectories induced by CAV and non-CAV FMT were accompanied by corresponding changes in microbial functional potential. A strong temporal and donor-group structure was observed (**Figure 10A**). Consistent with the taxonomic trajectories, all groups underwent a large early functional displacement after FMT but subsequently followed distinct trajectories in the taxa carrying these functions. We then identified pathways associated with the CAV and non-CAV post-FMT states using mixed-effects models adjusting for sampling day and repeated measurements within mice. CAV-FMT recipients were enriched for pathways

involved in xyloglucan degradation, nitrate reduction and denitrification, and glycolysis, including xyloglucan degradation II, nitrate reduction I and VII, and multiple glycolytic pathways (**Supplemental Figure 18**). In contrast, pathways involved in mycothiol biosynthesis, ketogluconate metabolism, menaquinol biosynthesis, 1,4-dihydroxy-6-naphthoate biosynthesis, and dopamine degradation were reduced in CAV-FMT recipients. Non-CAV FMT established a distinct, rather than simply reciprocal, functional state characterized by enrichment of dTDP-N-acetylthomosamine biosynthesis, anhydromuropeptide recycling, plasmalogen degradation, and related cell-envelope and metabolic pathways. A simplified longitudinal heatmap further showed preferential emergence of the CAV-associated carbohydrate degradation, glycolytic, and nitrate-reduction program after FMT, whereas the reciprocal pathway set was preferentially retained or enriched in non-CAV recipients (**Figure 10B**). These findings defined a CAV-associated microbial functional state enriched for carbohydrate utilization and nitrate-linked respiratory potential, distinct from the cell-envelope and metabolic programs associated with non-CAV FMT.

Taxonomic attribution of the discriminating pathways showed that these functional differences were distributed across multiple community members rather than driven by a single taxon (**Figure 10C**). *Muribaculaceae* contributed prominently to CAV-associated glycolytic pathways, whereas xyloglucan degradation also involved *Bacteroidaceae* contributions and selected clostridial taxa. Conversely, several pathways enriched in the non-CAV-associated state contained *Streptococcus*, *Bacteroides*, and *Bifido* contributions, although unclassified taxa accounted for a substantial portion of the functional phenotype. Together, the taxonomic and functional

646 analyses indicated that human FMT redirected the recipient microbiome at the
647 community level, with the CAV-associated state characterized by coordinated
648 redistribution of metabolic functions across *Muribaculaceae*, *Bacteroidaceae*, clostridial
649 lineages, and other community members rather than expansion of a single
650 microorganism.

Discussion

This study identifies the tacrolimus-conditioned gut ecosystem as a modifiable component of chronic post-transplant injury. The reproducible emergence of *Muribaculaceae*-dominated communities after cardiac transplantation extends our prior observations across mechanistically distinct immunosuppressants [13, 14] and suggests that chronic immune suppression imposes a shared ecological pressure on the intestinal microbiome. *Muribaculaceae* expansion should not be interpreted as inherently pathogenic or as a single causal driver of graft injury. Rather, its repeated emergence may mark a drug-selected intestinal state in which altered nutrient availability, host defense, and microbial competition favor saccharolytic lineages adapted to complex dietary and host-derived carbohydrates[15-19]. The accompanying shift from early metabolic disruption to later accumulation of TMAO, PAGln, and related aromatic co-metabolites further suggests that this ecological succession has systemic biochemical consequences. Because several of these co-metabolic pathways have established effects on platelet and vascular biology[20-23], the data raises the possibility that chronic immunosuppression influences graft outcome through metabolic pathways not targeted by conventional alloimmune suppression. The current study does not establish that these metabolites cause CAV, but it proposes a model implicating the perturbation of the gut-systemic metabolic axis.

Bifido gavage provides an important conceptual counterpoint to this drug-selected state. Its major effect was not durable dominance, but redirection of the surrounding microbial community. Metagenomic functional data reinforces this interpretation. *Bifido*-associated pathway changes were distributed among multiple

674 endogenous lineages, indicating redistribution of community functional potential rather
675 than direct replacement of tacrolimus-associated functions by the gavaged strain. This
676 may explain how transient exposure to a relatively low-abundance bacterium can have
677 effects extending beyond its own metabolic repertoire. More broadly, these findings
678 argue that the biological activity of a candidate probiotic cannot be inferred solely from
679 its genome or abundance; its capacity to alter ecological relationships and redistribute
680 functions across the resident community may be equally important[28].
681 The intestinal mucosa is likely the first host compartment to exhibit this altered
682 ecosystem. The spatial transcriptomic data showed that the dominant response
683 occurred at the luminal-facing colonic surface where TAC-associated metabolic, innate-
684 sensing, stress, growth-regulatory, and remodeling programs converged. Rather than
685 viewing cholesterol, bile acid, peroxisomal, NF-κB, PI3K–AKT–mTOR-associated, and
686 TGF-β/BMP signatures as independent pathways, their spatial and temporal
687 convergence suggests a broader epithelial adaptation state. The apical epithelium
688 continuously senses microbial products, bile acids, dietary substrates, and redox
689 conditions; coordinated engagement of these programs may therefore reflect the
690 energetic and regulatory demands imposed by the tacrolimus-conditioned lumen. *Bifido*
691 attenuated much of this response but generally did not return it to baseline. At the same
692 time, mitochondrial respiratory and antioxidant programs were selectively reconfigured.
693 Future direct measurements of sterol flux, bile acid receptor signaling, ROS, and mTOR
694 activity will be required to resolve the upstream drivers of this transcriptional state. The
695 later ileal response was biologically distinct and further argues against a simple
696 restoration model. The mTORC1-associated signature is particularly intriguing because

intestinal crypt cells must coordinate nutrient sensing with biosynthesis, protein quality control, and lineage maintenance. However, transcriptomic enrichment of mTORC1-associated genes does not establish increased mTOR kinase activity or epithelial proliferation. Instead, the coupling of metabolic, ER-proteostatic, and fatty-acid oxidative programs suggests increased cellular capacity to accommodate sustained metabolic and secretory demands in crypt-proximal tissue. This interpretation provides a testable framework for future measurements of phospho-S6/4EBP1, metabolic flux, proliferation, and epithelial lineage dynamics. The ileal immunoglobulin program adds an immune dimension to this late response. In contrast to the absence of broad canonical T cell or conventional B cell activation signatures, *Bifido* selectively engaged a humoral program consistent with antibody-secreting-cell activity and polymeric IgA biology. This distinction is important. A microbiome intervention that broadly activates intestinal lymphocytes would be difficult to reconcile with graft protection, whereas selective enhancement of mucosal antibody responses could strengthen microbial containment and reshape host-microbe interactions without inflammatory activation. Visium cannot distinguish expansion of antibody-secreting cells from greater transcriptional output by existing cells, and direct measurement of luminal IgA and bacterial IgA coating will be needed. Nonetheless, the data suggests that *Bifido* changes not only epithelial adaptation, but also mucosal immunity deployed against the remodeled community. Overall, the intestinal response is spatially and temporally staged, consistent with changing microbial and metabolic inputs rather than a uniform epithelial effect of the administered strain.

These intestinal changes occurred in parallel with reorganization of lymphoid and graft microenvironments. The increased positioning of Foxp3^{+} Tregs within CR- and HEV-associated regions is particularly informative because immune regulation depends not only on cell abundance but also on where regulatory cells encounter incoming leukocytes and antigen-presenting cells. Similarly, preservation of laminin α4:α5 organization in the graft suggests that *Bifido*-associated protection extends to tissue architecture that regulates leukocyte localization and inflammatory remodeling. The present data does not establish a causal sequence from intestinal epithelial adaptation to LN organization and graft protection. However, they support a gut–lymphoid–graft model in which microbial and metabolic state influence the stromal and cellular niches in which alloimmune responses are organized. This model is consistent with our prior work linking microbiota, LN remodeling, and tolerance [26, 29] and shifts the mechanistic question from whether the microbiome “suppresses immunity” to how microbial states alter the tissue architecture and localization of immune regulation.

The human FMT experiments extend this ecological model beyond *Bifido*. The key observation is not simply that mice receiving CAV-associated microbiota developed a different taxonomic profile. Murine *Muribaculaceae* emerged from an endogenous reservoir, indicating that the donor-associated community altered recipient ecological selection rather than directly transferring the dominant lineage associated with the subsequent phenotype. This distinction may be highly relevant to transplantation, where antibiotic exposure, immunosuppressive drugs, diet, and host immunity continually reshape ecological niches. A patient's microbiome may therefore influence outcome

741 through its capacity to determine which organisms subsequently expand and which
742 community functions are maintained.
743 Overall, these findings establish the gut microbiome as a tractable target in
744 transplantation science. Future work could focus on several priorities. First, the
745 mechanism of *Bifido*-mediated protection needs to be dissected to enhance
746 translational potential. Key questions include whether protection depends on direct
747 immune signaling through dendritic cells and macrophages, and restoration of SCFA-
748 producing networks, tryptophan-kynurenine and AhR-GPR35 signaling, polyamine
749 metabolism, suppression of TMAO and PAGln pathways, or others. Second, the
750 intervention should be optimized. Repeated dosing, strain selection, rational consortia
751 with cross-feeding partners, prebiotic support, and postbiotic metabolite replacement
752 may produce effective and durable effects. The human FMT study is exploratory and is
753 influenced by antibiotic conditioning, donor representation, and host-specific selection.
754 Third, the metabolomic data is associative. Although TMAO, PAGln, 4PY, kynurenic
755 acid, polyamines, and aromatic metabolites are biologically plausible mediators, direct
756 causal testing is still needed using metabolite supplementation, metabolite depletion,
757 receptor blockade, and microbial mutants. Fourth, baseline-guided personalization can
758 be considered, using pre-intervention microbiome profiling to identify “primed” vs.
759 “unprimed” recipients and adjust dosing/strain selection[30, 31]. Overall, these findings
760 support development of microbiome-informed strategies to reduce chronic graft injury
761 without increasing systemic immunosuppressive burden.

Conclusion

Together, these findings establish post-transplant gut dysbiosis as a dynamic and targetable axis of chronic allograft injury. Chronic tacrolimus imposed a reproducible ecological and metabolic trajectory marked by *Muribaculaceae*-dominated dysbiosis, altered gut-systemic co-metabolism, spatially organized intestinal stress and adaptation, and progressive graft vascular injury. *Bifido* gavage redirected this drug-conditioned ecosystem at the community, metabolic, intestinal, and immune-organ levels, with parallel preservation of regulatory lymphoid and graft architecture and reduced vasculitis and fibrosis. Human-to-mouse FMT further showed that CAV-associated microbiota can impose distinct recipient ecological and functional states linked to adverse graft phenotypes, supporting the translational relevance of microbiome-mediated ecological selection. Thus, microbiome disruption is not merely a consequence of immunosuppression but a modifiable component of the post-transplant environment that may amplify chronic graft injury. These findings support development of safe microbiome-directed adjunctive strategies designed to reshape community function and host response, complement conventional immunosuppression, and improve long-term graft function.

Methods and Materials

Strain cultivation

B. pseudolongum strain UMB-MBP-01 was isolated from the feces of C57BL/6J mice through passages and screening on Bifidus Selective Medium (BSM) agar (Sigma-Aldrich, St. Louis, MO, USA), as previously described[32]. Both strains were initially grown anaerobically at 37°C for 3-5 days on Bifido Selective Media (BSM) agar plates (Millipore Sigma, Burlington, MA), from which a single colony was selected and grown in BSM broth (Millipore Sigma, 90273-500G-F) until stationary phase (up to 3 days). *Desulfovibrio desulfuricans subsp. desulfuricans* (ATCC27774) was purchased from ATCC and grown in ATCC Medium: 1249 Modified Baar's Medium (MBM) for sulfate reducers, which was made according to ATCC protocol. Cultures were initially incubated under anaerobic conditions for 5 days on Modified Baar's Medium agar plates, after which single colonies were chosen, transferred to liquid media, and incubated for up to 3 weeks.

Immunohistochemistry

PLN, mLN, cardiac allografts, colon segment, and small bowel segment (duodenal-jejunal junction) were excised, washed in cold PBS, and flushed with 50-50 PBS-OCT mixture (for intestine) before flash frozen in OCT (Sakura Finetek, Torrance, CA) in histology blocks on an isopentane bath over liquid nitrogen and then stored at -80°C. LN cryosections were cut in triplicate at 6-7 µm for LNs, 10 µm for intestine and cardiac allografts using a Microm HM 550 cryostat (Thermo Fisher Scientific, Waltham, MA). Sections attached to slides were fixed with cold acetone/methanol (1:1) solution

and washed in PBS buffer (Lonza, Morristown, NJ). Slides were blocked with 10% donkey serum for 1 hour, washed with PBS, then primary antibodies and isotype controls (**Supplementary Table 5)** were added to slides for 1 hour in a humidified chamber. Sections were washed with PBS again thenincubated with secondary antibodies for 60 minutes. Slides were mounted with ProLong Gold Antifade Mountant (Thermo Fisher Scientific, Waltham, MA) with or without DAPI and coverslipped. Images were acquired using an Accu-Scope EXC-500 fluorescent microscope (Nikon, Melville, NY) and analyzed with Volocity image analysis software (PerkinElmer, Waltham, MA). The percentage positive staining area and mean fluorescent intensity were quantified and multiplied together based on at least 2 independent experiments with 3 mice/group, 2-3 tissues/mouse, 3 sections/tissue, and 3–5 fields/section. For LN microarchitecture and Treg positioning, sections were stained for Foxp3, Lama4, and Lama5; cardiac allograft sections were stained for laminin α4 and laminin α5 , CD4, CD8, and Foxp3 with DAPI counterstain, and the laminin α4:α5 ratio was quantified.

Mice experiments

Female C57BL/6 (H-2^b) recipient mice and BALB/c (H-2^d) cardiac donors, 8 to 14 weeks of age, were purchased from The Jackson Laboratory (Bar Harbor, ME). All procedures involving mice were performed in accordance with the guidelines and regulations set by the Office of Animal Welfare Assurance of the University of Maryland School of Medicine, under the approved IACUC protocols AUP-00000766, 0518004, 0715001, 0121001. The experimental cohorts were generated over several approval cycles; these identifiers therefore represent successive approved protocols and renewals in force for the respective cohorts, rather than multiple concurrent approvals

for the same procedures. The study is reported in accordance with the ARRIVE 2.0 guidelines. To standardize the gut microbial starting point and permit bacterial engraftment, recipients received broad-spectrum antibiotics ad libitum in drinking water from day -7 to day -1 before transplantation. Antibiotics were USP grade or pharmaceutical secondary standard (all from MilliporeSigma): kanamycin sulfate (0.4 mg/ml), gentamicin sulfate (0.035 mg/ml), colistin sulfate (850 U/ml), metronidazole (0.215 mg/ml), and vancomycin hydrochloride (0.045 mg/ml), dissolved in vivarium drinking water. On day 0, recipients underwent fully allogeneic heterotopic (intra-abdominal) cardiac transplantation of a BALB/c donor heart, with microsurgical anastomosis of the donor ascending aorta and pulmonary artery to the recipient infrarenal aorta and inferior vena cava, as previously described [26, 27]. Beginning on day 0, all recipients received daily tacrolimus (3 mg/kg/day, subcutaneously) for the duration of the experiment to model maintenance immunosuppression. Immediately before transplantation on day 0, recipients received a single oral gavage of *Bifido* (UMB-MBP-01), *Desulfo* (ATCC27774), or an equal volume of sterile PBS (tacrolimus-only control, TAC).

During cardiac transplantation, anesthesia was induced with Ketamine (80-150 mg/kg) / Xylazine (8-15 mg/kg) IP; anesthetic depth was assessed bytoe pinch. Perioperative analgesia consisted of Buprenorphine (0.05-0.1mg/kg) IP or SC prior to surgery and every 8-12 hours for 3 days postoperatively. At study endpoints, mice were euthanized by carbon dioxide (CO2) narcosis at [chamber displacement rate], followed by cervical dislocation to confirm death. Fecal pellets were collected longitudinally from day 0 through day 40 (days 0, 3, 7, 14, 21, 28, and 40) into individual tubes using

aseptic technique and stored at -80 degrees C. At the early (day 3) and late (day 40) endpoints, mice were euthanized and mesenteric and peripheral (axillary, inguinal, cervical, and brachial) LNs, small and large intestine with luminal contents, serum, and cardiac allografts were harvested for downstream metagenomic, metabolomic, spatial-transcriptomic, histologic, and immunofluorescence analyses. The bacterial-supplementation experiment was performed in two independent cohorts under identical transplantation, antibiotic-conditioning, and tacrolimus conditions to assess reproducibility. Tacrolimus (USP grade, MilliporeSigma) was reconstituted in DMSO (USP grade, MilliporeSigma) at 20 mg/ml and diluted with absolute ethanol (USP grade, Decon Labs, King of Prussia, PA) to 1.5 mg/ml; the DMSO/ethanol stock was diluted 1:5 in sterile PBS for subcutaneous injection at 10 ul/g (3 mg/kg/day). There were no exclusions of mice from analysis.

Cardiac allograft histopathology and vascular scoring

Cardiac allografts were harvested on day 3 and day 40, OCT-embedded, and sectioned. Interstitial fibrosis was assessed on Masson's trichrome-stained sections and graded using a semiquantitative fibrosis score. Allograft vascular injury was scored on the same sections using the standardized cardiac allograft rejection vascular (vasculitis) scoring system, based on the extent of perivascular and intravascular lymphocytic infiltration and vessel-wall damage [32]. Infiltration was graded on a scale of 0-4 with 0 indicating no rejection, 1 indicating mild interstitial or perivascular infiltrate without necrosis, 2 indicating focal interstitial or perivascular infiltrate with necrosis, 3 indicating multifocal interstitial or perivascular infiltrate with necrosis, and 4 indicating widespread infiltrate with hemorrhage and/or vasculitis. Fibrosis was graded on a scale of 1-4 with 1

indicating minimal (<10% area), 2 indicating mild (10%-30% area), 3 indicating moderate (30%-50% area), and 4 indicating severe (>50% area). All sections were scored by an observer blinded to treatment group. 3 sections per cardiac allograft and 5 fields per section were analyzed.

Human-to-mouse fecal microbiota transfer

To assess the translational relevance of donor microbial state, stool was obtained from individual cardiac-transplant recipients with CAV) or with stable graft function without CAV, and from a healthy donor. Collection and use of human stool were reviewed and approved by the University of Maryland, Baltimore Institutional Review Board in written document (IRB protocol HP-00084901) and was conducted in accordance with the principles of the Declaration of Helsinki. Written informed consent was obtained for all participants. Donor stool was processed under anaerobic conditions and resuspended to prepare the FMT inoculum. C57BL/6 recipient mice were conditioned with the broad-spectrum antibiotic cocktail described above from day -7 to -1, followed by a washout period, and underwent fully allogeneic BALB/c cardiac transplantation on day 0. Recipients received human donor FMT by oral gavage immediately before transplantation and then weekly for 3 weeks (days 0, 7, 14, and 21) to promote sustained engraftment (CAV-FMT, n = 6 recipient mice; non-CAV-FMT, n = 5; healthy-control FMT, n = 4). Fecal pellets were collected at days 0, 7, 28, and 60 for metagenomic profiling, and cardiac allografts and lymphoid tissues were harvested for histologic and immunofluorescence analysis as described above.

Metagenomic sequencing and microbiome analyses

Harvested intestine tissues and luminal contents were stored immediately in DNA/RNA Shields (Zymo Research, Irvine, CA) to stabilize and protect the integrity of nucleic acids and minimize the need to immediately process or freeze specimens. The colon content from ~1cm colon tissue was used in DNA extraction. Metagenomic sequencing libraries were constructed from the same DNA using the Nextera XT Flex kit (Illumina) according to the manufacturer recommendations. Libraries were then pooled together in equimolar proportions and sequenced on a single Illumina NovaSeq 6000 S2 flow cell at the Genomic Resource Center of the Institute for Genome Sciences at the University of Maryland School of Medicine. The same DNA extraction, library preparation, and sequencing procedures were applied to fecal samples from the bacterial-supplementation and human-FMT experiments.

Metagenomic sequence reads were removed using BMTagger v3.101 [33] using a Genome Reference Consortium Mouse Build 39 of strain C57BL/6J (GRCm39) [34]. Sequence read pairs were removed even if only one of the reads matched to the mice genome reference. The Illumina adapter was trimmed, and quality assessment was performed using default parameters in fastp (v.0.21.0) [35]. The taxonomic composition of the microbiomes was established using Kraken2 (v.2020.12) [36] and Braken (v. 2.5.0) [37]using the comprehensive mouse gut metagenome catalog (CMGM) [38] to calculate the metagenomic taxonomic composition. The Phyloseq (v.1.34.0) R package [39] was used to generate the diversity plot and barplot. Metagenomic reads were functionally profiled using HUMAnN v4.0.0.alpha.1 [40]. Reads not assigned through nucleotide alignment against the HUMAnN ChocoPhlAn reference were subjected to translated alignment

against the HUMAnN v4-alpha EC-filtered UniRef90 database (uniref90_annotated_v4_alpha_ec_filtered) [41]. Gene-family abundances were mapped to enzymatic reactions and MetaCyc pathways to estimate community metabolic potential. Unstratified pathway and reaction tables were used to visualize pathway abundance trajectories, while stratified HUMAnN tables were used only to identify taxonomic contributors to selected functions.

Metabolome analyses

Metabolome profiling is through the Primary Metabolism 400 panel for detection and absolute quantitation of >400 polar metabolites using ultra-performance liquid chromatography electrospray ionization-tandem mass spectrometry in multiple reactions monitoring (MRM) mode (UPLC-MRM MS) at University of Victoria Metabolomics Innovation Center. ~10-30 mg of stool and 50ul of serum was weighed at the time of collection and stored at -80°C until shipped to vendor on dry ice. QC procedures included standards, sample blanks and internal controls that were evenly spaced among the samples analyzed. To reduce the influence of measurement noise, rigorous data pretreatment was performed according to validated procedures [42] and are as previously described[14, 25, 43]. The normalization procedures were performed using the combination of log base 10 transformation and data scaling via mean-centered and unit-variance scaled per metabolite. For each metabolite, group differences were assessed by one-way analysis of variance. Pairwise post hoc comparisons were performed using Tukey's honestly significant difference (HSD) test. To account for multiple hypothesis testing across all metabolites, raw ANOVA p-values were adjusted using the Benjamini-Hochberg false discovery rate (FDR) procedure. Metabolites with FDR-adjusted p <

0.05 were considered significantly different across groups. Partial least squares discriminant analysis (PLS-DA) was performed using mixOmics[44], with the first two components retained (ncomp = 2). The percentage of total variance explained by each component was extracted from the fitted model and reported on the corresponding biplot axes. Sample relationships were additionally visualized by hierarchical clustering and principal-component analysis, and longitudinal changes were modeled with group-by-day linear models spanning the day-0 (post-antibiotic) baseline and the day-3 and day-40 post-gavage time points, as detailed under Statistical analysis.

Spatial transcriptomics of ileal and colonic tissues using 10x Genomics

Ileal and colonic tissues were collected at the indicated early (day 3) and late (day 40) post-transplant time points, embedded in OCT, snap-frozen, and stored at -80 degrees C until sectioning. Fresh-frozen tissue blocks were cryosectioned at 10 µm onto 10x Genomics Visium Spatial Gene Expression slides according to the manufacturer's fresh-frozen tissue preparation workflow, which is designed to preserve both tissue morphology and RNA integrity for downstream spatial transcriptomic profiling. Tissue sections were fixed, H&E-stained, and imaged before library preparation according to the manufacturer's demonstrated protocols (CG000160, CG000239, and CG000240). Brightfield images were acquired using an Invitrogen EVOS M700 imaging system with Celleste software version 6.0. Each capture area was inspected to confirm tissue integrity, epithelial orientation, and adequate coverage of ileal or colonic mucosa. Spatial gene expression libraries were prepared using the 10x Genomics Visium Spatial Gene Expression workflow. Briefly, fixed and stained tissue sections were permeabilized to release polyadenylated mRNA, which was captured by

960 oligo-dT primers printed on spatially barcoded capture spots. Tissue permeabilization
961 was optimized at 12 minutes for both colon and ileum based on the manufacturer's
962 Tissue Optimization protocol (CG000238). On-slide reverse transcription generated
963 spatially indexed cDNA, followed by cDNA amplification, library construction, and
964 sample indexing. Libraries were sequenced on an Illumina NovaSeq 6000 platform,
965 targeting 50,000 read pairs per tissue-covered spot, in accordance with 10x Genomics
966 guidance.
967 Sequencing reads were processed using Space Ranger count v2.0.1 with the
968 10x Genomics mouse reference transcriptome refdata-gex-mm10-2020-A. H&E images
969 were aligned to the Visium capture areas, and gene expression matrices were
970 generated for each tissue section. Samples from each intestinal site, ileum and colon,
971 were then aggregated separately using Space Ranger *aggr*. For spatial analysis, ileal
972 and colonic sections were analyzed independently. Visium spots were assigned to
973 apical or basal epithelial compartments using k-means clustering with k=2, followed by
974 visual inspection against tissue morphology to confirm layer assignment. Differential
975 gene expression analysis was performed using DESeq2 to compare apical and basal
976 epithelial regions between treatment groups and time points.
977 Raw per-spot counts were extracted from the .cloupe files and summed per
978 biological mouse by merging technical-replicate sections where the same mouse was
979 sectioned onto two slides x compartment. Counts were CPM-normalized and log1p-
980 transformed. For PCA and clustering, genes with mean log-CPM > 1 were retained
981 (9,912 of 32,287) and the top 2,000 most variable genes were used, z-scored per gene.
982 For module scoring, 50 MSigDB hallmark gene sets [45] were scored per sample as the

mean per-gene z-score of each gene set's member genes present in the data. For each gene and each Hallmark module score, we fitted a linear model with compartment, tissue, and treatment group as categorical predictors. To estimate the relative contribution of each factor, we calculated the reduction in residual sum of squares attributable to that factor after accounting for the other two factors, equivalent to partial Type-II sums of squares for a main-effects model. The variance explained by each factor was then expressed as a percentage of the total model-attributable variance. STRING functional-association networks were generated for the significant genes within each selected module restricted to *Mus musculus*. Returned interactions were filtered using the STRING combined confidence score, retaining edges with score ≥0.4 for gene sets with more than eight genes and score ≥0.15 for smaller gene sets to avoid empty networks. Networks were constructed in *networkx*, with all queried genes retained as nodes, including unconnected genes.

Statistical analysis

Community structure was assessed by principal-coordinate analysis of Bray-Curtis dissimilarities, with group and time effects tested by permutational multivariate analysis of variance (PERMANOVA; *vegan::adonis2, model ~ group + day*). Alpha diversity (Shannon index) was modeled with linear mixed-effects models including group, scaled day, experiment, and a per-mouse random intercept (*lme4/lmerTest*). For targeted longitudinal differential-abundance testing, taxon relative abundances were arcsine-square-root transformed and fitted with linear mixed-effects models including group, scaled day, and experiment as fixed effects and mouse as a random intercept, with the PBS/tacrolimus-only group as the reference; multiple testing was controlled by

the Benjamini-Hochberg FDR within taxonomic rank and time phase. HUMAnN pathway and reaction abundances were modeled with linear mixed-effects models (*nlme::lme*) including day and experiment (and treatment group where applicable); pathways reaching FDR < 0.10 in both cohorts were considered replicated, and a treatment-by-experiment interaction FDR < 0.20 was used to indicate experiment-specific effects. Taxonomic contributions to selected functions were derived from stratified HUMAnN output. For the metabolome, group differences at each time point were tested by one-way ANOVA with Tukey HSD post hoc comparisons and Benjamini-Hochberg FDR correction, and temporal effects were assessed with longitudinal group-by-day linear models spanning the shared day-0 (post-antibiotic) baseline and the day-3 and day-40 post-gavage time points. For spatial transcriptomics, per-mouse pseudobulk profiles were compared with DESeq2, and 50 MSigDB Hallmark module scores were computed per sample; the relative contributions of epithelial compartment, tissue type, and treatment group to each gene and module score were estimated by variance partitioning (partial type-II sums of squares). STRING functional-association networks were constructed for significant module genes restricted to Mus musculus (species 10090), retaining edges with a combined confidence score >= 0.4 (relaxed to >= 0.15 for gene sets with <= 8 members) and visualized with *networkx*. Two-sided FDR-adjusted p < 0.05 was considered statistically significant unless otherwise specified.

References

1. Kobashigawa JA, Tobis JM, Starling RC, Tuzcu EM, Smith AL, Valantine HA, et al. Multicenter intravascular ultrasound validation study among heart transplant recipients: outcomes after five years. J Am Coll Cardiol 2005; 45:1532–7.
2. Mehra MR, Crespo-Leiro MG, Dipchand A, Ensminger SM, Hiemann NE, Kobashigawa JA, et al. International Society for Heart and Lung Transplantation working formulation of a standardized nomenclature for cardiac allograft vasculopathy-2010. J Heart Lung Transplant 2010; 29:717–27.
3. Colvin M, Smith JM, Ahn Y, Skeans MA, Messick E, Goff R, et al. OPTN/SRTR 2019 Annual Data Report: Heart. Am J Transplant 2021; 21 Suppl 2:356–440.
4. Pober JS, Chih S, Kobashigawa J, Madsen JC, Tellides G. Cardiac allograft vasculopathy: current review and future research directions. Cardiovasc Res 2021; 117:2624–38.
5. Tuzcu EM, Kapadia SR, Tutar E, Ziada KM, Hobbs RE, McCarthy PM, et al. High prevalence of coronary atherosclerosis in asymptomatic teenagers and young adults: evidence from intravascular ultrasound. Circulation 2001; 103:2705–10.
6. Fishman JA. Infection in Organ Transplantation. Am J Transplant 2017; 17:856–79.
7. Bhat M, Usmani SE, Azhie A, Woo M. Metabolic Consequences of Solid Organ Transplantation. Endocr Rev 2021; 42:171–97.
8. Lund LH, Khush KK, Cherikh WS, Goldfarb S, Kucheryavaya AY, Levvey BJ, et al. The Registry of the International Society for Heart and Lung Transplantation: Thirty-fourth Adult Heart Transplantation Report-2017; Focus Theme: Allograft ischemic time. J Heart Lung Transplant 2017; 36:1037–46.
9. Costanzo MR, Dipchand A, Starling R, Anderson A, Chan M, Desai S, et al. The International Society of Heart and Lung Transplantation Guidelines for the care of heart transplant recipients. J Heart Lung Transplant 2010; 29:914–56.
10. Gabarre P, Loens C, Tamzali Y, Barrou B, Jaisser F, Tourret J. Immunosuppressive therapy after solid organ transplantation and the gut microbiota: Bidirectional interactions with clinical consequences. Am J Transplant 2022; 22:1014–30.
11. Faucher Q, Jardou M, Brossier C, Picard N, Marquet P, Lawson R. Is Intestinal Dysbiosis-Associated With Immunosuppressive Therapy a Key Factor in the Pathophysiology of Post-Transplant Diabetes Mellitus? Front Endocrinol (Lausanne) 2022; 13:898878.
12. Kensiski A, Gavzy SJ, Wu L, Mas V, Ma B, Bromberg JS. Immunosuppressant imprecision: multidirectional effects on metabolism and microbiome. Clin Microbiol Rev 2025; 38:e0017824.
13. Wu L, Kensiski A, Gavzy SJ, Song Y, Lwin HW, France M, et al. Immunosuppressants rewire the gut microbiome-alloimmune axis through time-dependent and tissue-specific mechanisms. Cell Commun Signal 2025; 23:506.
14. Wu L, Kensiski A, Gavzy SJ, Lwin HW, Song Y, France MT, et al. Rapamycin immunomodulation utilizes time-dependent alterations of lymph node architecture, leukocyte trafficking, and gut microbiome. JCI Insight 2025; 10.
15. Ormerod KL, Wood DL, Lachner N, Gellatly SL, Daly JN, Parsons JD, et al. Genomic characterization of the uncultured Bacteroidales family S24-7 inhabiting the guts of homeothermic animals. Microbiome 2016; 4:36.

16. Lagkouvardos I, Lesker TR, Hitch TCA, Galvez EJC, Smit N, Neuhaus K, et al. Sequence and cultivation study of Muribaculaceae reveals novel species, host preference, and functional potential of this yet undescribed family. Microbiome 2019; 7:28.
17. Smith BJ, Miller RA, Schmidt TM. Muribaculaceae Genomes Assembled from Metagenomes Suggest Genetic Drivers of Differential Response to Acarbose Treatment in Mice. mSphere 2021; 6:e0085121.
18. Yang X, Wang Z, Niu J, Zhai R, Xue X, Wu G, et al. Pathobionts from chemically disrupted gut microbiota induce insulin-dependent diabetes in mice. Microbiome 2023; 11:62.
19. Chang TT, Chen JW. Direct CCL4 Inhibition Modulates Gut Microbiota, Reduces Circulating Trimethylamine N-Oxide, and Improves Glucose and Lipid Metabolism in High-Fat-Diet-Induced Diabetes Mellitus. J Inflamm Res 2021; 14:6237–50.
20. Wang Z, Klipfell E, Bennett BJ, Koeth R, Levison BS, Dugar B, et al. Gut flora metabolism of phosphatidylcholine promotes cardiovascular disease. Nature 2011; 472:57–63.
21. Zhu W, Gregory JC, Org E, Buffa JA, Gupta N, Wang Z, et al. Gut Microbial Metabolite TMAO Enhances Platelet Hyperreactivity and Thrombosis Risk. Cell 2016; 165:111–24.
22. Nemet I, Saha PP, Gupta N, Zhu W, Romano KA, Skye SM, et al. A Cardiovascular Disease-Linked Gut Microbial Metabolite Acts via Adrenergic Receptors. Cell 2020; 180:862–77 e22.
23. Ferrell M, Wang Z, Anderson JT, Li XS, Witkowski M, DiDonato JA, et al. A terminal metabolite of niacin promotes vascular inflammation and contributes to cardiovascular disease risk. Nat Med 2024; 30:424–34.
24. Zelante T, Iannitti RG, Cunha C, De Luca A, Giovannini G, Pieraccini G, et al. Tryptophan catabolites from microbiota engage aryl hydrocarbon receptor and balance mucosal reactivity via interleukin-22. Immunity 2013; 39:372–85.
25. Ma B, Gavzy SJ, Saxena V, Song Y, Piao W, Lwin HW, et al. Strain-specific alterations in gut microbiome and host immune responses elicited by tolerogenic Bifidobacterium pseudolongum. Sci Rep 2023; 13:1023.
26. Bromberg JS, Hittle L, Xiong Y, Saxena V, Smyth EM, Li L, et al. Gut microbiota-dependent modulation of innate immunity and lymph node remodeling affects cardiac allograft outcomes. JCI Insight 2018; 3.
27. Staley C, Kaiser T, Beura LK, Hamilton MJ, Weingarden AR, Bobr A, et al. Stable engraftment of human microbiota into mice with a single oral gavage following antibiotic conditioning. Microbiome 2017; 5:87.
28. France MT, Fu L, Rutt L, Yang H, Humphrys MS, Narina S, et al. Insight into the ecology of vaginal bacteria through integrative analyses of metagenomic and metatranscriptomic data. Genome Biol 2022; 23:66.
29. Gavzy SJ, Kensiski A, Saxena V, Lakhan R, Hittle L, Wu L, et al. Early Immunomodulatory Program Triggered by Protolerogenic Bifidobacterium pseudolongum Drives Cardiac Transplant Outcomes. Transplantation 2024.
30. Ianiro G, Puncochar M, Karcher N, Porcari S, Armanini F, Asnicar F, et al. Variability of strain engraftment and predictability of microbiome composition after fecal microbiota transplantation across different diseases. Nat Med 2022; 28:1913–23.
31. Podlesny D, Fricke WF. Strain inheritance and neonatal gut microbiota development: A meta-analysis. Int J Med Microbiol 2021; 311:151483.

32. Mongodin EF, Hittle LL, Nadendla S, Brinkman CC, Xiong Y, Bromberg JS. Complete Genome Sequence of a Strain of Bifidobacterium pseudolongum Isolated from Mouse Feces and Associated with Improved Organ Transplant Outcome. Genome Announc 2017; 5.
33. Rotmistrovsky K, Agarwala R, B. BMTagger: Best Match Tagger for removing human reads from metagenomics datasets. Integrative Human Microbiome Project (iHMP) by NCBI/NLM, National Institutes of Health, 2011.
34. Church DM, Schneider VA, Graves T, Auger K, Cunningham F, Bouk N, et al. Modernizing reference genome assemblies. PLoS Biol 2011; 9:e1001091.
35. Chen S, Zhou Y, Chen Y, Gu J. fastp: an ultra-fast all-in-one FASTQ preprocessor. Bioinformatics 2018; 34:i884–i90.
36. Wood DE, Lu J, Langmead B. Improved metagenomic analysis with Kraken 2. Genome Biol 2019; 20:257.
37. Lu J, Breitwieser FP, Thielen P, SL S. Bracken: estimating species abundance in metagenomics data. PeerJ Computer Science 2017; 3:e104.
38. Kieser S, Zdobnov EM, Trajkovski M. Comprehensive mouse gut metagenome catalog reveals major difference to the human counterpart. bioRxiv 2021:2021.03.18.435958.
39. McMurdie PJ, Holmes S. phyloseq: an R package for reproducible interactive analysis and graphics of microbiome census data. PLoS One 2013; 8:e61217.
40. Beghini F, McIver LJ, Blanco-Miguez A, Dubois L, Asnicar F, Maharjan S, et al. Integrating taxonomic, functional, and strain-level profiling of diverse microbial communities with bioBakery 3. Elife 2021; 10.
41. Kanehisa M, Goto S, Sato Y, Furumichi M, Tanabe M. KEGG for integration and interpretation of large-scale molecular data sets. Nucleic Acids Res 2012; 40:D109–14.
42. van den Berg RA, Hoefsloot HC, Westerhuis JA, Smilde AK, van der Werf MJ. Centering, scaling, and transformations: improving the biological information content of metabolomics data. BMC Genomics 2006; 7:142.
43. Ma B, Gavzy SJ, France M, Song Y, Lwin HW, Kensiski A, et al. Rapid intestinal and systemic metabolic reprogramming in an immunosuppressed environment. BMC Microbiol 2023; 23:394.
44. Rohart F, Gautier B, Singh A, Le Cao KA. mixOmics: An R package for 'omics feature selection and multiple data integration. PLoS Comput Biol 2017; 13:e1005752.
45. Liberzon A, Birger C, Thorvaldsdottir H, Ghandi M, Mesirov JP, Tamayo P. The Molecular Signatures Database (MSigDB) hallmark gene set collection. Cell Syst 2015; 1:417–25.

Ethical Approval and Consent to participate

All animal procedures were reviewed and approved by the Institutional Animal Care and Use Committee (IACUC) of the University of Maryland School of Medicine under protocols 0715001, 0518004, 0121001, and AUP-00000766. These identifiers correspond to successive approval and renewal cycles covering experimental cohorts conducted during different phases of this multi-year study. Human stool collection and use were approved by the University of Maryland, Baltimore Institutional Review Board (protocol HP-00084901).

Availability of data and materials

All sequencing data and attached metadata will be submitted to GenBank under BioProject PRJNA809764 Microbiome-driven cardiac allograft outcomes" upon acceptance. Metabolome data were deposited to NGDC OMIX repository (OMIX ID: OMIX022296 under BioProject PRJCA077480).

Declaration of interests

B.M. and J.S.B. are inventors on pending U.S. Patent Application No. 19/543,131, published as US 2026/0240870 A1, entitled 'Methods of Reducing Transplant Rejection in Subjects Undergoing Immunosuppressant Therapy'; all other authors declare no competing financial or non-financial interests.

Funding

This work was supported by the National Institute of Health (NIH) National Heart, Lung and Blood Institute award R01HL148672 (JSB/BM), NIH National Institute of Allergy and Infectious Diseases U01AI170050 (BM/JSB/VM), R01AI114496 (JSB), R01AI189709 (JSB/BM), and training grant T32AI95190-10 (SJG). University of Maryland Baltimore ORD-OTT No. BM-2025-077.

Authors' contributions

B. M., A. K., L. W., S. J. G., J. B. designed the experiments. A. K., L. W., S. J. G., T. Z., M. W., B. L., W. P. conducted and analyzed the *in vitro* and *in vivo* experiments. H. W. L. performed DNA extraction. B. M. and I. C. performed the bioinformatics analyses. B. M., A. K., L. W. performed the statistical analyses. B. M., A. K., L. W., S. J. G., I. C., M. F., V. R. M., and J. S. B. wrote the manuscript. B. M., J. S. B. are co-corresponding authors for this manuscript.

Figure 1. Tacrolimus induces ordered taxonomic succession and coordinated remodeling of microbial functional potential after cardiac transplantation. (**A**) Longitudinal relative-abundance trajectories of major bacterial families in fecal metagenomes from cardiac-allograft recipients maintained on daily tacrolimus. Faceted plots show family-specific changes from day 0 to day 40. (**B**) Mean family-level trajectories. Points and lines show group means; error bars indicate variability among mice. (**C**) Longitudinal HUMAnN4 pathway and reaction profiles showing progressive depletion of D-lactate dehydrogenase, kynurenine 3-monooxygenase, polyamine biosynthesis I, hexitol fermentation to lactate/formate/acetate, NAD salvage to nicotinamide riboside, and tryptophan synthase activity. (**D**) Representative carbohydrate-processing pathways retained or enriched during the later *Muribaculaceae*-dominant phase. (**E**) Stratified taxonomic contributions to glycolysis III from glucose across the longitudinal time course.

Figure 2. Chronic tacrolimus is associated with temporally staged intestinal and systemic metabolic remodeling after cardiac transplantation. Ileal intraluminal and serum metabolites profiled at day 0, after antibiotic conditioning but before transplantation and tacrolimus initiation, and at days 3 and 40 after cardiac transplantation under daily tacrolimus treatment. Partial least squares discriminant analysis (PLS-DA) of (**A**) ileal intraluminal and (**B**) serum metabolomes showing distinct time-dependent metabolic states. Samples colored by collection day; ellipses show group dispersion, and labeled vectors indicate representative metabolites contributing to separation along the first two components. Representative metabolites in (**C**) intraluminal stool, and (**D**) serum. Coordinated gut-systemic remodeling after cardiac transplantation in E) choline-trimethylamine (TMA)-trimethylamine N-oxide (TMAO) pathway and F) PAA-PAGln pathways. Differences across time points assessed by one-way ANOVA with Tukey HSD post hoc pairwise comparisons and Benjamini-Hochberg correction across metabolites. Significant pairwise differences: $P < 0.05$, $P < 0.01$, $P < 0.001$, and $P < 0.0001$. Metabolic pathway schematics created with BioRender.com (https://BioRender.com/mj6r03n).

Figure 3. *Bifidobacterium pseudolongum* (*Bifido*) redirects the tacrolimus-conditioned gut microbiome after cardiac transplantation. (**A**) Experimental design. Antibiotic-conditioned C57BL/6 mice underwent fully allogeneic cardiac transplantation and received daily tacrolimus together with oral gavage of *Bifidobacterium pseudolongum subsp globosum* (*Bifido*), *Desulfovibrio desulfuricans* (*Desulfo*), or PBS control (tacrolimus-only, TAC). Fecal samples collected longitudinally from day 0 through day 40. (**B**) Longitudinal Bray-Curtis principal coordinate trajectories of fecal microbial communities. (**C**) Principal component analysis of taxonomic profiles with selected genus-level vectors. Points colored by sampling day and enclosed by treatment-group. (**D**) Longitudinal relative abundance of *Bifido* and major *Muribaculaceae* genera. (**E**) Forest plot showing families and genera associated with *Bifidobacterium* abundance. Associations estimated using linear mixed-effects models adjusted for day, treatment group, and experiment and mouse as a random intercept. P values corrected within each taxonomic rank using the Benjamini–Hochberg method. Points denote -log10 Benjamini-Hochberg FDR, horizontal lines indicate 95% confidence intervals, and only taxa with intervals not crossing zero displayed. *Bifidobacterium* excluded to avoid part-whole correlations.

Figure 4. Functional consequences of *Bifido* intervention under chronic tacrolimus exposure for two independent mouse cohorts HUMAnN4 pathway profiles. (**A**) Row-scaled heatmap of shared pathways defined by a pooled FDR < 0.10 and concordant Bifido versus control effect direction in both cohorts. Mean log-transformed pathway abundance calculated by treatment, cohort, and day; red and blue indicate relatively higher and lower abundance, respectively. (**B**) Adjusted *Bifido*-versus-PBS pathway effects from the mixed-effects model. Positive coefficients indicate higher abundance in *Bifido*-treated mice and negative coefficients indicate higher abundance in TAC controls; point size represents −log10 FDR. (**C**) Taxonomic attribution using stratified HUMAnN4 profiles. Bars show each contributor group's signed fraction of the absolute stratified

pathway difference; positive and negative values indicate contributions to higher pathway abundance in *Bifido* and TAC controls, respectively.

Figure 5. *Bifido* establishes a distinct luminal metabolic program under chronic tacrolimus treatment. PLS-DA biplots of FDR-significant stool metabolites at day 3 (**A**) and day 40 (**B**) after *Bifido*, *Desulfo*, or PBS control (TAC, tacrolimus-only) gavage. Points represent individual mice (n=3/group), ellipses indicate group enclosure, and vectors show metabolite loading direction and magnitude. Normalized abundance of (**C**) day-3 and (**D**) Day-40 discriminatory metabolites. Brackets indicate Tukey-adjusted pairwise comparisons. (**E**) Longitudinal trajectories of kynurenic acid and N-acetylspermine from the shared day-0 post-antibiotic baseline through days 3 and 40. Points and lines show group means ± SEM. $P < 0.01$, $P < 0.001$, and $P < 0.0001$.

Figure 6. Spatial transcriptomics identifies Bifido-associated reprogramming of the early colonic apical metabolic response. Principal component analysis of mouse-level pseudobulk spatial transcriptomic profiles, colored by (**A**) epithelial compartment using PC1 and PC2 or (**B**) sampling time point using PC3 and PC4. (**C**) Representative Visium tissue sections showing spatial assignment of apical (red) and basal (blue) compartments based on transcriptomic clustering and tissue localization for both colon and ileum. (**D**) Gene-level differential-expression profiles for cholesterol homeostasis, peroxisome, bile acid metabolism, and reactive oxygen species (ROS) modules in the colonic apical compartment at day 3. For each module, rows show TAC versus *Bifido* (top) and TAC versus pretreatment baseline (bottom). Dot color indicates log2 fold change, with red denoting higher expression in TAC and blue lower expression in TAC; dot size represents −log10 Benjamini-Hochberg-adjusted P value.

Figure 7. *Bifido* elicits spatially and program-specific intestinal transcriptional responses under chronic tacrolimus treatment. (**A**) Gene-level differential-expression profiles of TNFα signaling via NF-κB module and the TGF-β/BMP signaling module in the colonic apical compartment at day 3. (**B**) Antimicrobial-defense and IgA and plasma-cell secretory programs in the ileal apical compartment at day 40. (**C**) mTORC1-associated transcriptional program in the ileal basal compartment at day 40. For A-C, rows show TAC versus *Bifido* (top) and TAC versus pretreatment baseline (bottom). Dot color indicates log2 fold change, with red denoting higher expression in TAC and blue lower expression in TAC; dot size represents −log10 Benjamini-Hochberg-adjusted *P* value. STRING functional-association networks of (**D**) TGF-β signaling genes in the colonic apical compartment at day 3 and (**E**) mTORC1-associated genes in the ileal basal compartment at day 40. Each node split to show log2 fold change for TAC versus pretreatment baseline (left) and TAC versus *Bifido* (right); red indicates higher expression in TAC and blue lower expression in TAC. Node size reflects −log10 adjusted *P* value, and edge width reflects STRING association confidence. (**F**) Spatial distribution of the colonic contractile-remodeling module at day 40 across pretreatment baseline, TAC, and *Bifido*-treated tissues. Module scores highest near the muscularis boundary. (**G**) Spatial distribution of the IgA/plasma-cell secretory module across ileal tissue at day 40. Spatial maps show mean log1p(CP10K) module scores across Visium spots.

Figure 8. *Bifido* mitigates graft vasculitis and preserves regulatory lymphoid and graft stromal organization during chronic tacrolimus treatment. (**A**) Representative histologic sections and scoring of cardiac allograft inflammation and fibrosis in TAC control, *Bifido*-, and *Desulfo*-treated mice at days 3 and 40. Fibrosis assessed on Masson's trichrome-stained sections. (**B**) Representative graft vessels and vascular injury scores assessed using the cardiac graft-rejection vascular grading system based on the severity and distribution of perivascular and intravascular lymphocytic infiltration and vessel-wall injury [4]. (**C**) Quantification of $Foxp3^+$ Treg localization within cortical ridge (CR) and high endothelial venule (HEV) regions of mesenteric lymph nodes (mLNs) and peripheral lymph nodes (pLNs) at days 3 and 40. Representative staining shown in Supplemental Figure 15. (**D**) Intragraft stromal and immune remodeling assessed by the laminin

α4:α5 ratio and quantification of $CD4^+$, $Foxp3^+$, and $CD8^+$ T-cell infiltration at days 3 and 40. Approximately 10 fields evaluated per section, and scores averaged across fields for each section. Scale bar, 100 μm.

Figure 9. Human CAV-associated microbiota promotes graft injury and lymphoid stromal remodeling and establishes distinct post-FMT microbial trajectories. (**A**) Experimental design. Antibiotic-conditioned cardiac allograft recipients received stool microbiota from cardiac transplant patients with and without CAV or a healthy donor, followed by four weekly FMT administrations and continuous immunosuppression. (**B**) Cardiac allograft fibrosis scores and quantification of intragraft $CD4^+$ and $CD8^+$ T-cell staining. (**C**) IHC for laminin α4:α5 ratios in CR and HEV regions of pLNs. Unpaired Student's t tests. (**D**) Representative H&E- and Masson's trichrome-stained cardiac allograft sections. (**E**) Representative graft vessels showing perivascular and intravascular lymphocytic infiltration used for histologic assessment of graft vasculitis. Scale bars, 100 μm. (**F**) Longitudinal whole-community microbiome trajectories based on Bray–Curtis dissimilarity and principal-coordinate analysis. Lines connect repeated samples from the same mouse at days 0, 7, 28, and 60, with collection day indicated within each point. All groups showed pronounced early community displacement followed by distinct post-FMT trajectories and relatively similar late community states at days 28 and 60. (**G**) Longitudinal relative-abundance trajectories of CAG-873, *Duncaniella*, Muribaculaceae, and *Bifidobacterium*. Thin lines show individual mice; thick lines show group means and error bars indicate mean ± SE.

Figure 10. CAV-associated microbiota establishes distinct functional states after human FMT. (**A**) Longitudinal trajectories of taxon-stratified microbial functional profiles derived from HUMAnN pathway-by-taxon contributions. Stratified features detected in at least 10% of samples retained, and the top 700 features by combined abundance and variance rank analyzed by Bray-Curtis principal-coordinate analysis. Points represent individual samples and lines connect group centroid trajectories across days 0, 7, 28, and 60. (**B**) Longitudinal heatmap of selected CAV- and non-CAV-associated microbial pathways. For each pathway, log10-transformed relative abundance z-scored across samples and averaged within each FMT group and time point. Upper block pathways enriched in the CAV-associated post-FMT state; lower block reciprocal pathways enriched in non-CAV or reduced in CAV. Red and blue indicate higher and lower row-scaled abundance, respectively. (**C**) Taxonomic attribution of selected discriminatory pathways using stratified HUMAnN profiles. Stacked bars show the post-FMT difference in pathway contribution between CAV-FMT recipients and the combined non-CAV/healthy-control groups, partitioned among major taxonomic contributors.

Figure 1.

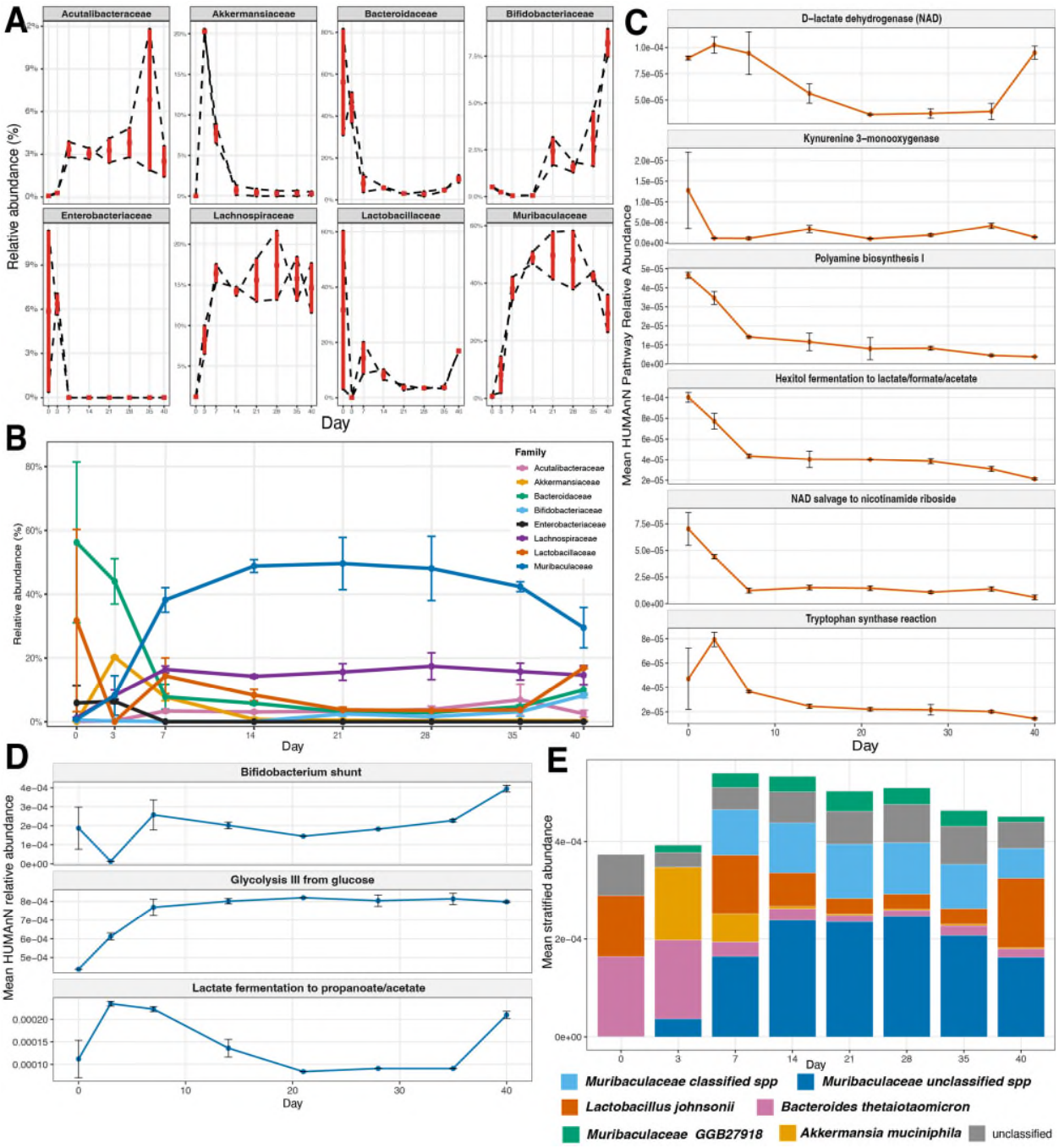

A
Acutalibacteraceae
Akkermansiaceae
Bacteroidaceae
Bifidobacteriaceae
Enterobacteriaceae
Lachnospiraceae
Lactobacillaceae
Muribaculaceae
Relative abundance (%)
Day
B
Family
Acutalibacteraceae
Akkermansiaceae
Bacteroidaceae
Bifidobacteriaceae
Enterobacteriaceae
Lachnospiraceae
Lactobacillaceae
Muribaculaceae
Relative abundance (%)
Day
C
D-lactate dehydrogenase (NAD)
Kynurenine 3-monooxygenase
Polyamine biosynthesis I
Hexitol fermentation to lactate/formate/acetate
NAD salvage to nicotinamide riboside
Tryptophan synthase reaction
Mean HUMAnN Pathway Relative Abundance
Day
D
Bifidobacterium shunt
Glycolysis III from glucose
Lactate fermentation to propanoate/acetate
Mean HUMAnN relative abundance
Day
E
Mean stratified abundance
Day
Muribaculaceae classified spp
Muribaculaceae unclassified spp
Lactobacillus johnsonii
Bacteroides thetaiotaomicron
Muribaculaceae GGB27918
Akkermansia muciniphila
unclassified

Figure 2

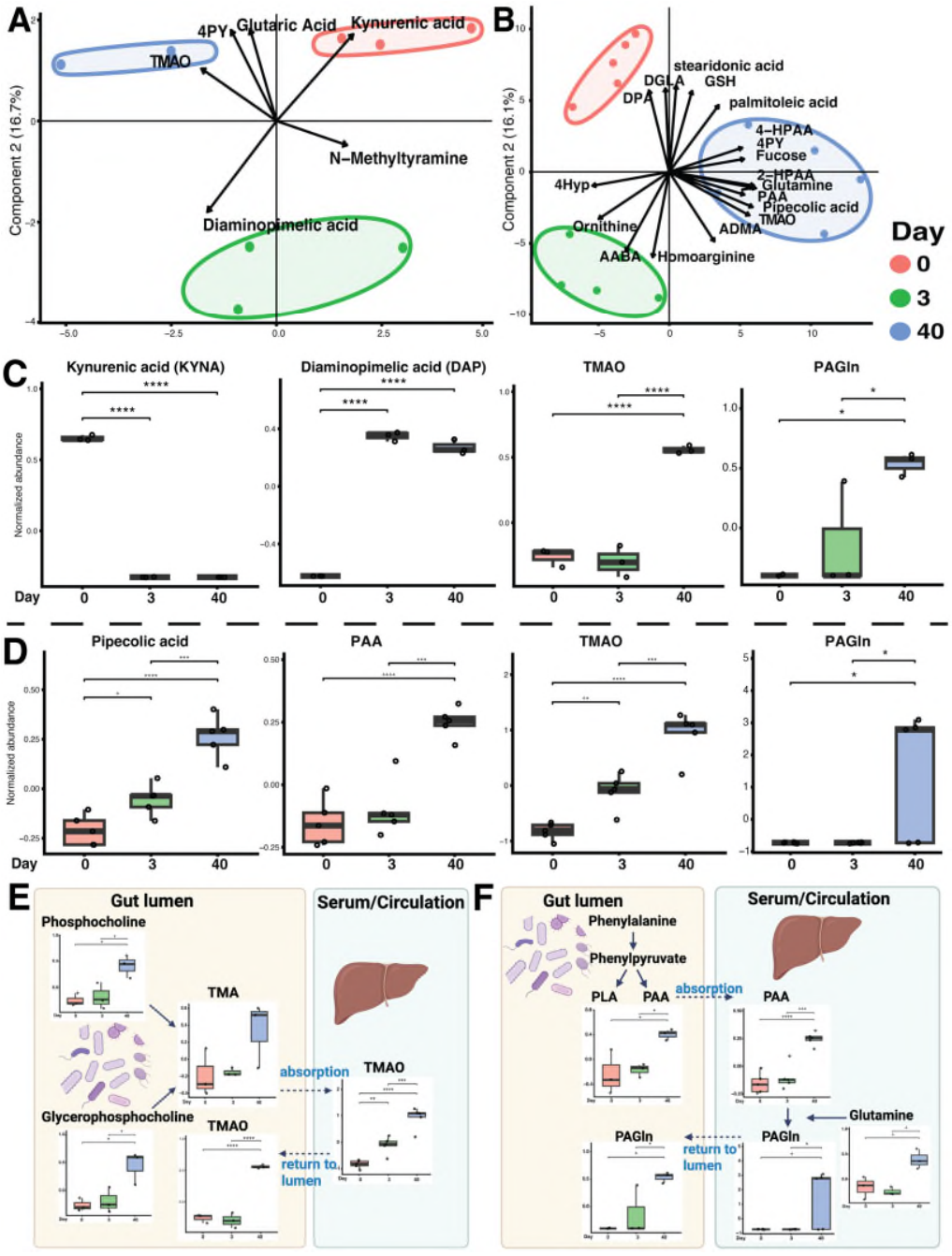

A
4PY
Glutaric Acid
Kynurenic acid
TMAO
N−Methyltyramine
Diaminopimelic acid
Component 2 (16.7%)
B
stearidonic acid
DGLA
GSH
DPA
palmitoleic acid
4−HPAA
4PY
Fucose
2−HPAA
Glutamine
PAA
Pipecolic acid
TMAO
4Hyp
Ornithine
ADMA
AABA
Homoarginine
Component 2 (16.1%)
Day
0
3
40
C
Kynurenic acid (KYNA)
Diaminopimelic acid (DAP)
TMAO
PAGln
Normalized abundance
Day
D
Pipecolic acid
PAA
TMAO
PAGln
E
Gut lumen
Serum/Circulation
Phosphocholine
TMA
Glycerophosphocholine
TMAO
absorption
return to lumen
F
Gut lumen
Serum/Circulation
Phenylalanine
Phenylpyruvate
PLA
PAA
absorption
Glutamine
PAGln
return to lumen

Figure 3

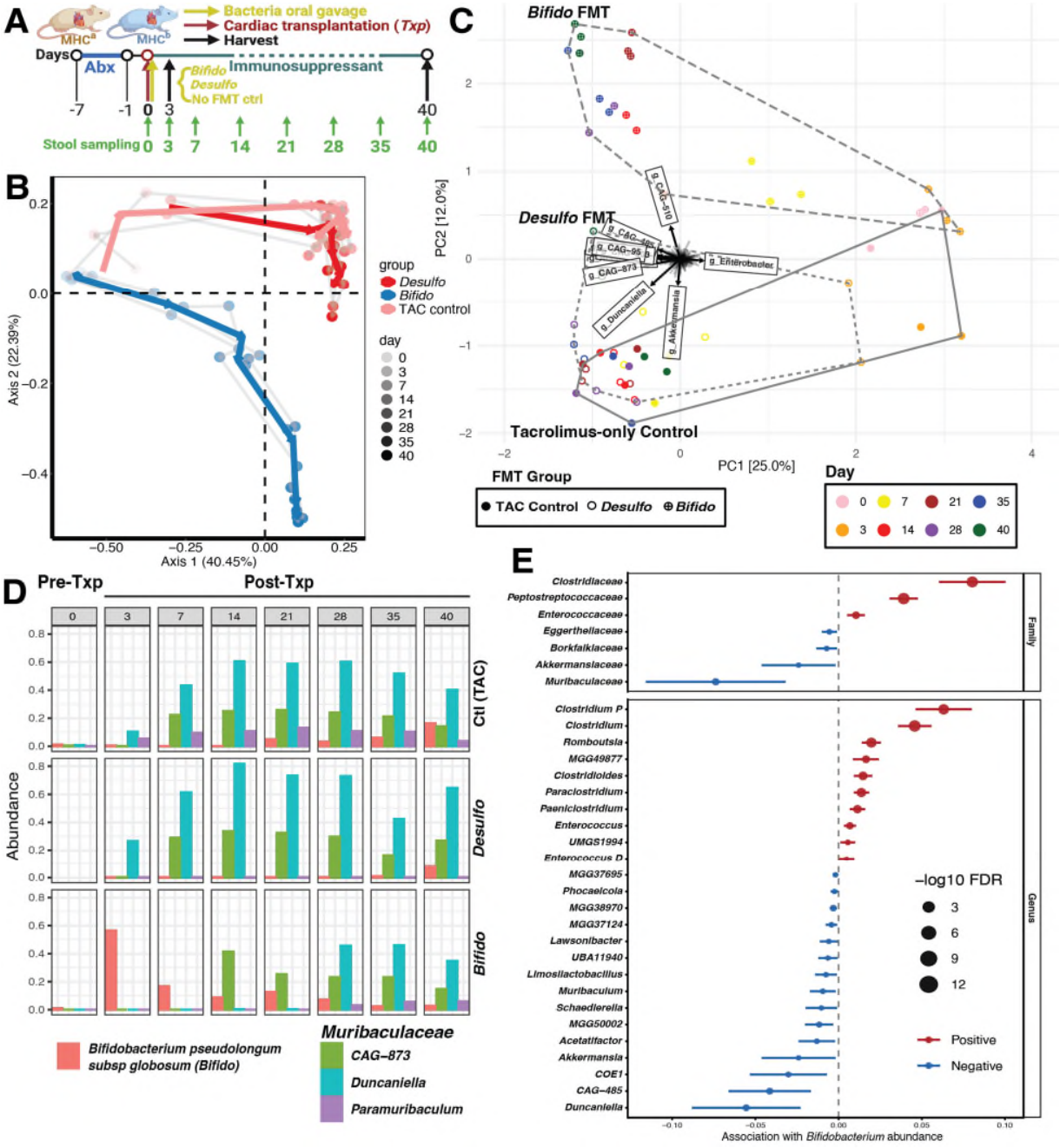

A
MHC^a
MHC^b
Bacteria oral gavage
Cardiac transplantation (Txp)
Harvest
Days
Abx
Immunosuppressant
Bifido
Desulfo
No FMT ctrl
-7
-1
0
3
40
Stool sampling 0 3 7 14 21 28 35 40
B
Axis 2 (22.39%)
Axis 1 (40.45%)
group
Desulfo
Bifido
TAC control
day
0
3
7
14
21
28
35
40
C
Bifido FMT
Desulfo FMT
Tacrolimus-only Control
g_CAG-310
g_CAG-485
g_CAG-95
g_CAG-873
g_Enterobacter
g_Duncaniella
g_Akkermansia
PC2 [12.0%]
PC1 [25.0%]
FMT Group
TAC Control
Desulfo
Bifido
Day
D
Pre-Txp
Post-Txp
Ctl (TAC)
Desulfo
Bifido
Abundance
Bifidobacterium pseudolongum subsp globosum (Bifido)
Muribaculaceae
CAG-873
Duncaniella
Paramuribaculum
E
Clostridiaceae
Peptostreptococcaceae
Enterococcaceae
Eggerthellaceae
Borkfalkiaceae
Akkermansiaceae
Muribaculaceae
Family
Clostridium P
Clostridium
Romboutsia
MGG49877
Clostridioides
Paraclostridium
Paeniclostridium
Enterococcus
UMGS1994
Enterococcus D
MGG37695
Phocaeicola
MGG38970
MGG37124
Lawsonibacter
UBA11940
Limosilactobacillus
Muribaculum
Schaedlerella
MGG50002
Acetatifactor
Akkermansia
COE1
CAG-485
Duncaniella
Genus
-log10 FDR
3
6
9
12
Positive
Negative
Association with Bifidobacterium abundance

Figure 4

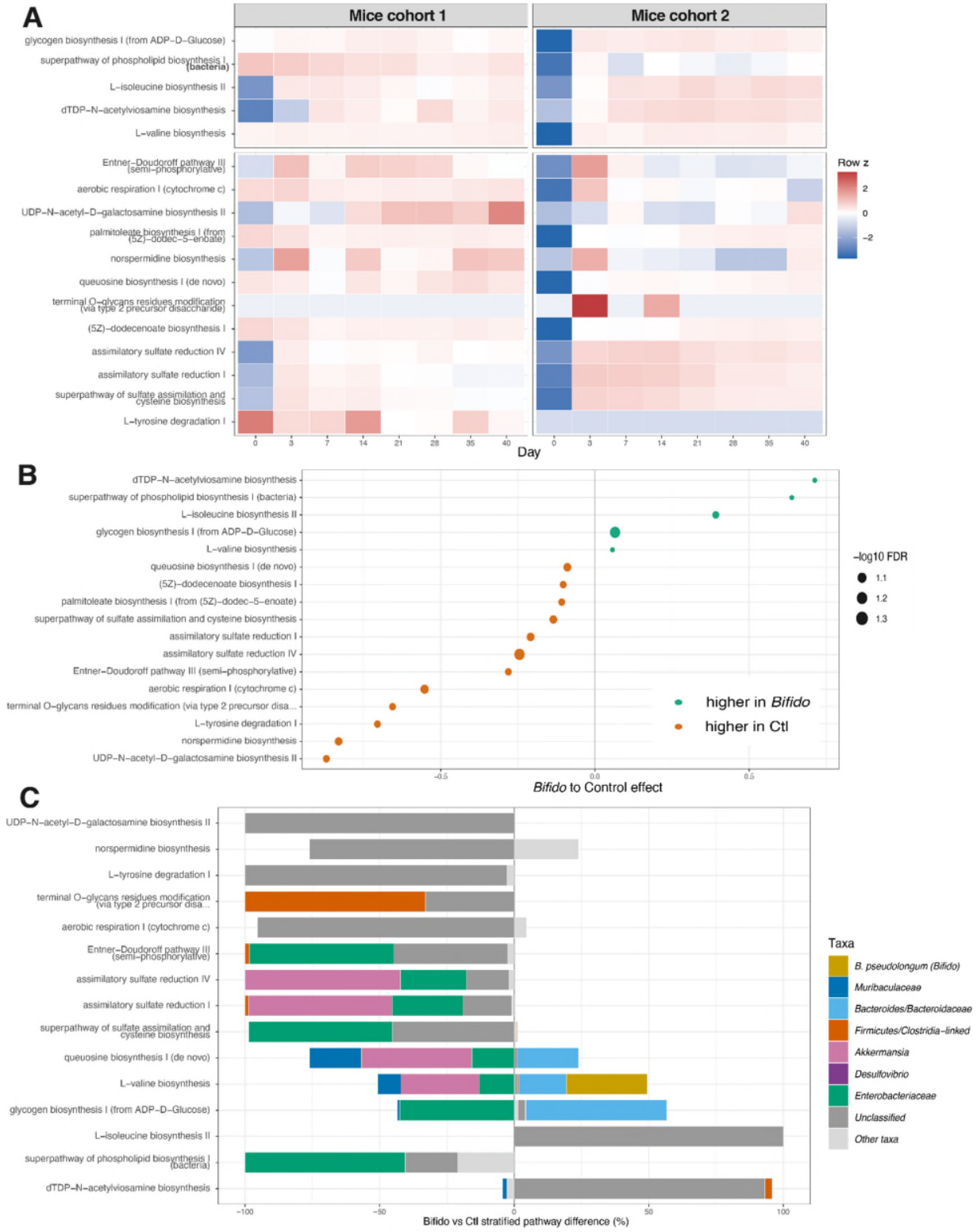

A
Mice cohort 1
Mice cohort 2
glycogen biosynthesis I (from ADP-D-Glucose)
superpathway of phospholipid biosynthesis I (bacteria)
L-isoleucine biosynthesis II
dTDP-N-acetylviosamine biosynthesis
L-valine biosynthesis
Entner-Doudoroff pathway III (semi-phosphorylative)
aerobic respiration I (cytochrome c)
UDP-N-acetyl-D-galactosamine biosynthesis II
palmitoleate biosynthesis I (from (5Z)-dodec-5-enoate)
norspermidine biosynthesis
queuosine biosynthesis I (de novo)
terminal O-glycans residues modification (via type 2 precursor disaccharide)
(5Z)-dodecenoate biosynthesis I
assimilatory sulfate reduction IV
assimilatory sulfate reduction I
superpathway of sulfate assimilation and cysteine biosynthesis
L-tyrosine degradation I
0 3 7 14 21 28 35 40
Day
Row z
2
0
−2
B
dTDP-N-acetylviosamine biosynthesis
superpathway of phospholipid biosynthesis I (bacteria)
L-isoleucine biosynthesis II
glycogen biosynthesis I (from ADP-D-Glucose)
L-valine biosynthesis
queuosine biosynthesis I (de novo)
(5Z)-dodecenoate biosynthesis I
palmitoleate biosynthesis I (from (5Z)-dodec-5-enoate)
superpathway of sulfate assimilation and cysteine biosynthesis
assimilatory sulfate reduction I
assimilatory sulfate reduction IV
Entner-Doudoroff pathway III (semi-phosphorylative)
aerobic respiration I (cytochrome c)
terminal O-glycans residues modification (via type 2 precursor disa...
L-tyrosine degradation I
norspermidine biosynthesis
UDP-N-acetyl-D-galactosamine biosynthesis II
higher in Bifido
higher in Ctl
−0.5 0.0 0.5
Bifido to Control effect
−log10 FDR
1.1
1.2
1.3
C
UDP-N-acetyl-D-galactosamine biosynthesis II
norspermidine biosynthesis
L-tyrosine degradation I
terminal O-glycans residues modification (via type 2 precursor disa...
aerobic respiration I (cytochrome c)
Entner-Doudoroff pathway III (semi-phosphorylative)
assimilatory sulfate reduction IV
assimilatory sulfate reduction I
superpathway of sulfate assimilation and cysteine biosynthesis
queuosine biosynthesis I (de novo)
L-valine biosynthesis
glycogen biosynthesis I (from ADP-D-Glucose)
L-isoleucine biosynthesis II
superpathway of phospholipid biosynthesis I (bacteria)
dTDP-N-acetylviosamine biosynthesis
−100 −50 0 50 100
Bifido vs Ctl stratified pathway difference (%)
Taxa
B. pseudolongum (Bifido)
Muribaculaceae
Bacteroides/Bacteroidaceae
Firmicutes/Clostridia-linked
Akkermansia
Desulfovibrio
Enterobacteriaceae
Unclassified
Other taxa

Figure 5

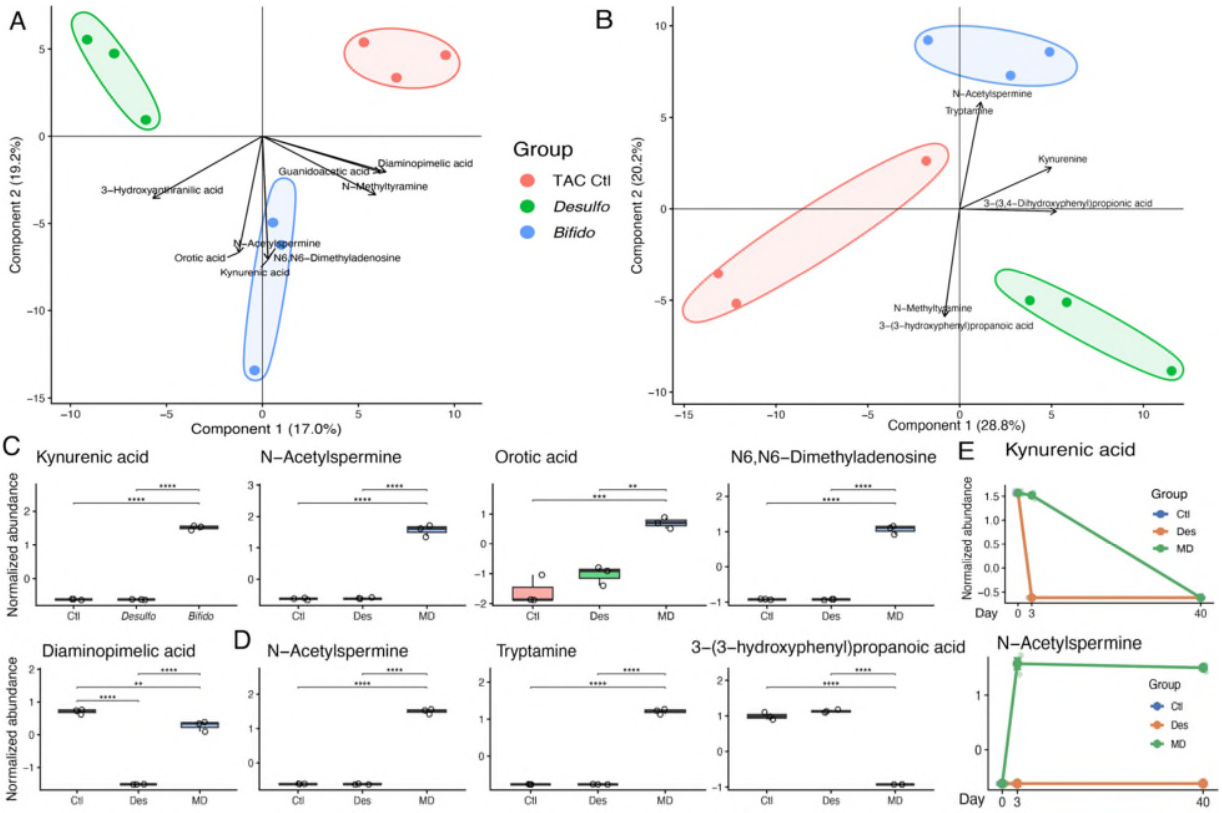

A
Component 2 (19.2%)
Component 1 (17.0%)
3−Hydroxyanthranilic acid
Guanidoacetic acid
Diaminopimelic acid
N−Methyltyramine
N−Acetylspermine
Orotic acid
N6,N6−Dimethyladenosine
Kynurenic acid
Group
TAC Ctl
Desulfo
Bifido
B
Component 2 (20.2%)
Component 1 (28.8%)
N−Acetylspermine
Tryptamine
Kynurenine
3−(3,4−Dihydroxyphenyl)propionic acid
N−Methyltyramine
3−(3−hydroxyphenyl)propanoic acid
C
Kynurenic acid
N−Acetylspermine
Orotic acid
N6,N6−Dimethyladenosine
Normalized abundance
Ctl
Desulfo
Bifido
Des
MD
D
Diaminopimelic acid
N−Acetylspermine
Tryptamine
3−(3−hydroxyphenyl)propanoic acid
E
Kynurenic acid
N−Acetylspermine
Group
Ctl
Des
MD
Day
0
3
40

Figure 6

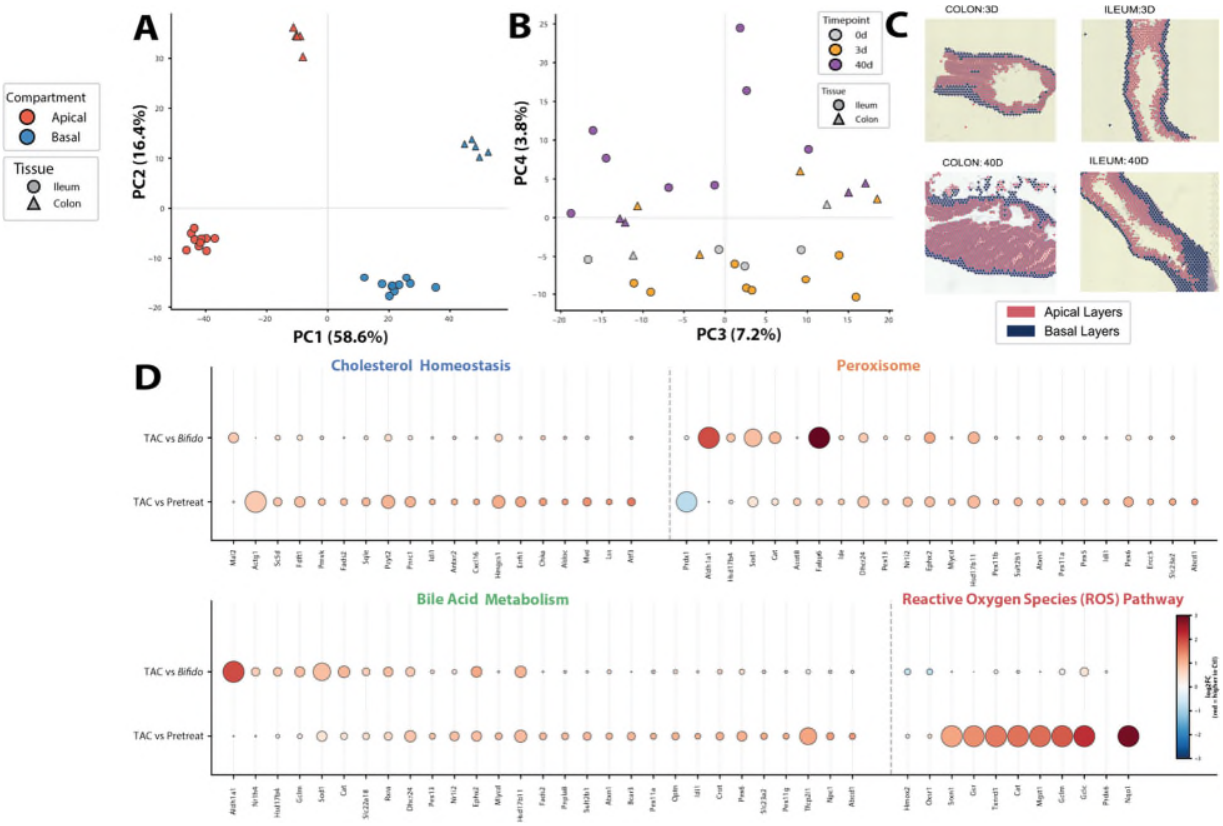

Compartment
Apical
Basal
Tissue
Ileum
Colon
A
PC2 (16.4%)
PC1 (58.6%)
B
PC4 (3.8%)
PC3 (7.2%)
Timepoint
0d
3d
40d
Tissue
Ileum
Colon
C
COLON:3D
ILEUM:3D
COLON: 40D
ILEUM: 40D
Apical Layers
Basal Layers
D
Cholesterol Homeostasis
Peroxisome
TAC vs Bifido
TAC vs Pretreat
Bile Acid Metabolism
Reactive Oxygen Species (ROS) Pathway

Figure 7

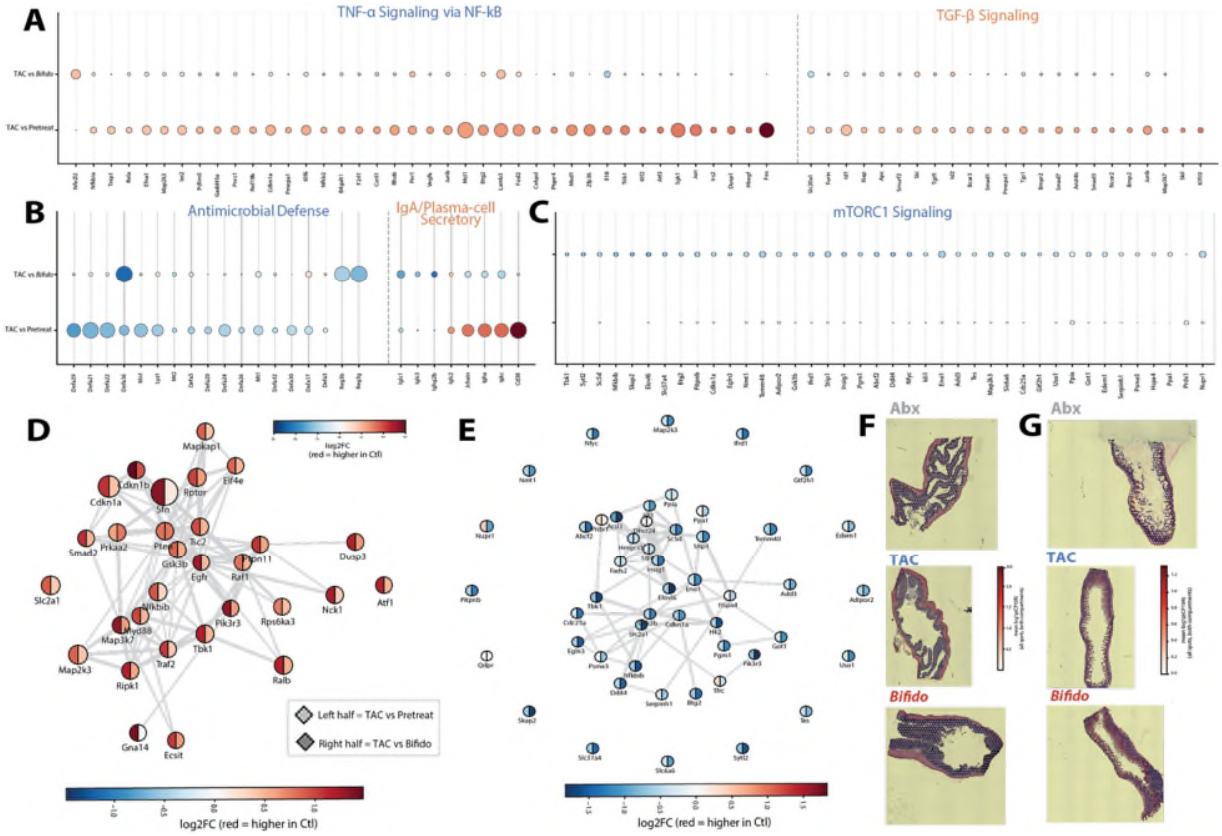

A
TNF-α Signaling via NF-kB
TGF-β Signaling
TAC vs Bifido
TAC vs Pretreat
B
Antimicrobial Defense
IgA/Plasma-cell Secretory
C
mTORC1 Signaling
D
E
F
G
Abx
TAC
Bifido
log2FC (red = higher in Ctl)
Left half = TAC vs Pretreat
Right half = TAC vs Bifido

Figure 8

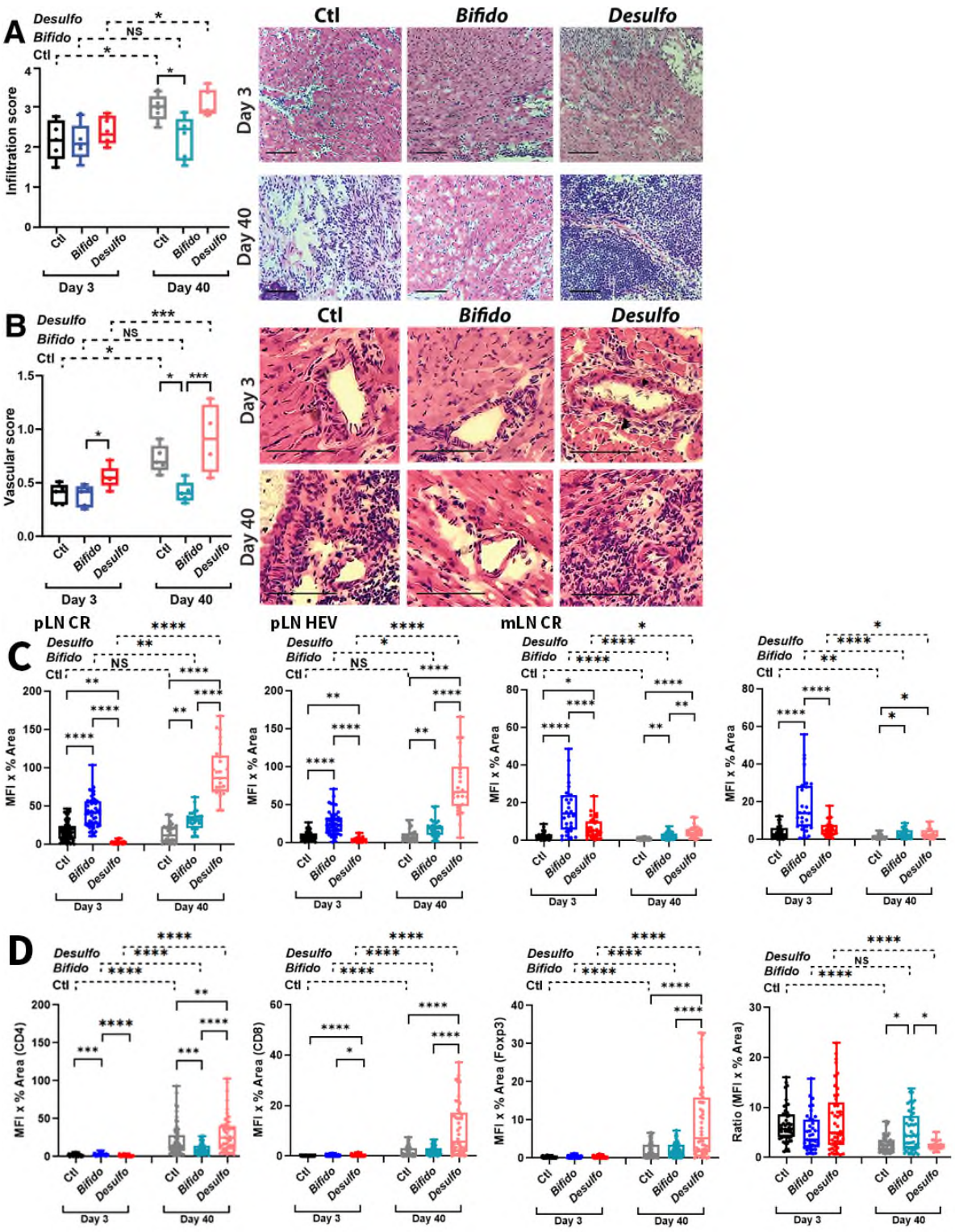

A
Desulfo
Bifido
Ctl
NS
Infiltration score
Day 3
Day 40
Ctl
Bifido
Desulfo
B
Vascular score
C
pLN CR
pLN HEV
mLN CR
MFI x % Area
D
MFI x % Area (CD4)
MFI x % Area (CD8)
MFI x % Area (Foxp3)
Ratio (MFI x % Area)

Figure 9

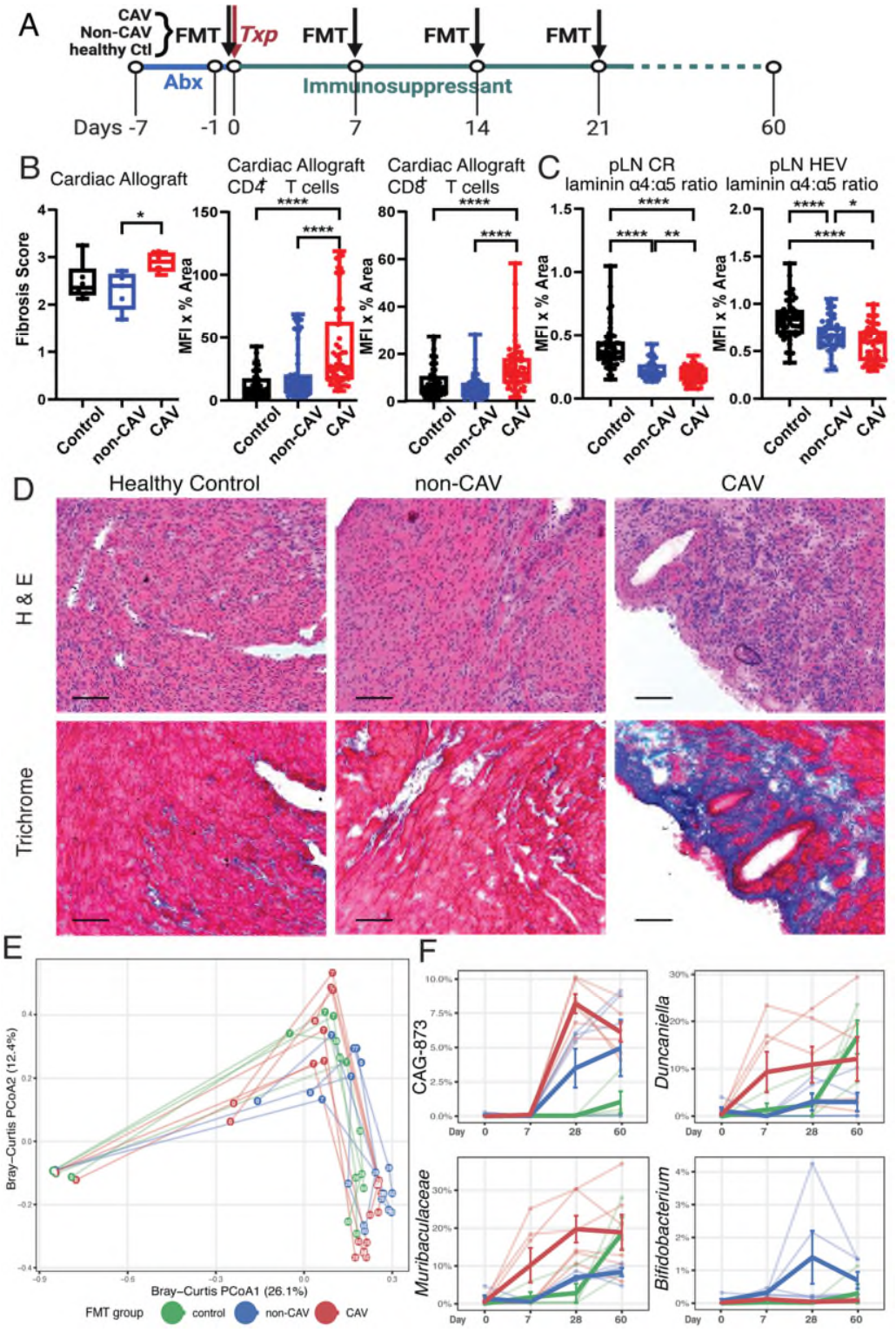
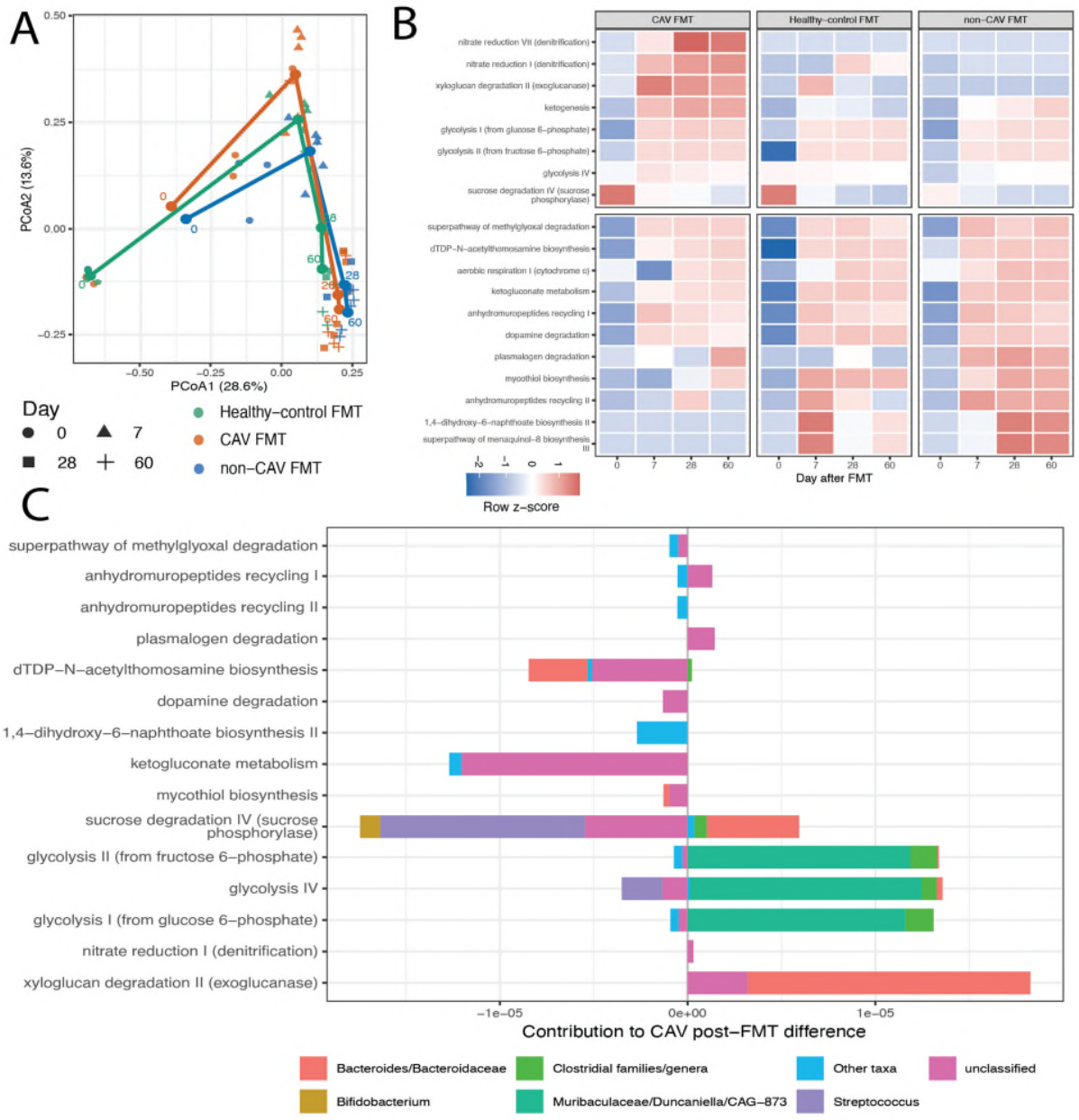

A
CAV
Non-CAV
healthy Ctl
FMT
Txp
FMT
FMT
FMT
Abx
Immunosuppressant
Days -7
-1
0
7
14
21
60
B
Cardiac Allograft
Fibrosis Score
Cardiac Allograft
CD4+ T cells
MFI x % Area
Cardiac Allograft
CD8+ T cells
MFI x % Area
C
pLN CR
laminin α4:α5 ratio
MFI x % Area
pLN HEV
laminin α4:α5 ratio
MFI x % Area
Control
non-CAV
CAV
D
Healthy Control
non-CAV
CAV
H & E
Trichrome
E
Bray–Curtis PCoA2 (12.4%)
Bray–Curtis PCoA1 (26.1%)
FMT group
control
non-CAV
CAV
F
CAG-873
Duncaniella
Muribaculaceae
Bifidobacterium
Day

Figure 10


A
PCoA2 (13.6%)
PCoA1 (28.6%)
Day
0
7
28
60
Healthy−control FMT
CAV FMT
non−CAV FMT
B
CAV FMT
Healthy−control FMT
non−CAV FMT
nitrate reduction VII (denitrification)
nitrate reduction I (denitrification)
xyloglucan degradation II (exoglucanase)
ketogenesis
glycolysis I (from glucose 6−phosphate)
glycolysis II (from fructose 6−phosphate)
glycolysis IV
sucrose degradation IV (sucrose phosphorylase)
superpathway of methylglyoxal degradation
dTDP−N−acetylthomosamine biosynthesis
aerobic respiration I (cytochrome c)
ketogluconate metabolism
anhydromuropeptides recycling I
dopamine degradation
plasmalogen degradation
mycothiol biosynthesis
anhydromuropeptides recycling II
1,4−dihydroxy−6−naphthoate biosynthesis II
superpathway of menaquinol−8 biosynthesis III
Row z−score
Day after FMT
C
superpathway of methylglyoxal degradation
anhydromuropeptides recycling I
anhydromuropeptides recycling II
plasmalogen degradation
dTDP−N−acetylthomosamine biosynthesis
dopamine degradation
1,4−dihydroxy−6−naphthoate biosynthesis II
ketogluconate metabolism
mycothiol biosynthesis
sucrose degradation IV (sucrose phosphorylase)
glycolysis II (from fructose 6−phosphate)
glycolysis IV
glycolysis I (from glucose 6−phosphate)
nitrate reduction I (denitrification)
xyloglucan degradation II (exoglucanase)
−1e−05
0e+00
1e−05
Contribution to CAV post−FMT difference
Bacteroides/Bacteroidaceae
Clostridial families/genera
Other taxa
unclassified
Bifidobacterium
Muribaculaceae/Duncaniella/CAG−873
Streptococcus

Supplementary Files

This is a list of supplementary files associated with this preprint. Click to download.

- S1.xlsx
- S2.xlsx
- S3.xlsx
- S4.xlsx
- SupplementalFigurelegendv3.docx